An MRI Compatible Manipulator for Prostate Cancer Detection and Treatment

by

Lauren M. DeVita

Bachelor of Engineering in Mechanical Engineering
The Cooper Union for the Advancement of Science and Art, 2005

Submitted to the Department of Mechanical Engineering
in partial fulfillment of the requirements for the degree of
Master of Science in Mechanical Engineering

at the

Massachusetts Institute of Technology

May 2007

Signature of Author . . . . . .
Department of Mechanical Engineering
May 15, 2007

Certified by . . . . . .
Steven Dubowsky
Professor of Mechanical Engineering
Thesis Supervisor

Accepted by . . . . . .
Professor Lallit Anand
Chairman, Committee on Graduate Studies

An MRI Compatible Manipulator for Prostate Cancer Detection and Treatment

by

Lauren M. DeVita

Submitted to the Department of Mechanical Engineering
on May 15, 2007, in partial fulfillment of the
requirements for the degree of
Master of Science in Mechanical Engineering

ABSTRACT

Prostate cancer is the most frequently diagnosed cancer in men and the second most common cause of cancer related death in men. Prostate specific antigen (PSA) blood tests and digital rectal exams (DRE) are preliminary tests that can suggest the presence of prostate cancer. Following these tests, a needle biopsy is required to determine if a suspected tumor is benign or malignant. Currently, an ultrasound image is used to help guide a needle to the prostate and to the suspected region. However, ultrasound images are not of good enough quality to accurately hit a tumor. Too often, false negative results are returned because the tumor is missed.

This can be prevented by using more accurate images, which can be obtained using Magnetic Resonance Imaging (MRI). This presents a technical challenge because it requires robotic assistance since there is very limited access to a patient inside the bore. Additionally, the high magnetic fields prohibit the use of conventional actuators in the procedure.

Dielectric Elastomer Actuators (DEAs) are MRI compatible due to their entirely polymer construction. Studies show that DEAs must be actuated in a bistable manner to be reliable. In this thesis, bistable DEAs were used in the design of an MRI compatible robotic needle manipulator. The concepts of elastic averaging and parallel mechanisms were applied to achieve high precision and adequate stiffness.

The manipulator parameters were chosen to fit the specifications established with collaborators at Harvard Medical School's Brigham and Women's Hospital. A design to orient the needle has been developed, analyzed and built.

This research shows that the design is feasible for development into a clinical device if manufacturing processes allow for fabrication of multi-layer actuators. Calculations and experiments show repeatability, precision and MRI compatibility.

Thesis Supervisor: Steven Dubowsky, Professor of Mechanical Engineering

ACKNOWLEDGEMENTS

The past two years at MIT have been an incredible journey and a learning experience unlike no other. I would like to thank the many people who have guided me along the way:

- Professor Steven Dubowsky, for sharing your knowledge and expertise and for always pushing me to achieve more than I think I can.
- All of the members of the Field and Space Robotics Laboratory, especially Dr. Jean-Sebastien Plante for his continual support and advice, Sam Kesner and Chris Ward for the hours of 'babysitting' in the machine shop, and Dr. Kenjiro Tadakuma for building so many functional actuators.
- The entire MIT staff and faculty for an amazing educational experience and Cooper Union for preparing me to take on this challenge.
- Dan Kacher, Dr. Simon DiMaio, Dr. Joseph Roebuck and Dr. Clare Tempany at Brigham and Women's Hospital for their collaboration and encouragement.
- My friends for keeping me sane and out of trouble.

Most importantly, I would like to thank my family for always believing in me. You are my greatest source of inspiration and my motivation.

I dedicate this work in loving memory of my grandfather Poppy, Grandma Connie and Uncle Louie.

TABLE OF CONTENTS

LIST OF FIGURES

LIST OF TABLES

CHAPTER

1

INTRODUCTION

1.1 Motivation

Despite the number of tumors that go undetected, prostate cancer is the most frequently diagnosed cancer in men. It is predicted that 218,890 men will be diagnosed in 2007 alone [22]. One in six men will be diagnosed with prostate cancer in his lifetime. Cancer deaths from prostate cancer in men, about 30,000 a year, are second only to lung cancer [21]. The estimated 27,050 deaths in 2007 is a number that has been declining since the early 1990s due to better detection and treatment methods [22].

The first and most crucial step in prostate cancer treatment is diagnosis. Doctors can successfully find signs of the disease through preliminary tests, such as Prostate Specific Antigen (PSA) blood tests and Digital Rectal Exams (DRE). They have far more difficulty confirming if a tumor is actually present and whether it is benign or malignant. Every year, about 800,000 men have a prostate biopsy [36]. Of these, about 75% have negative results (no cancer is found). Studies show that current biopsy techniques miss up to 20% of prostate cancers [2,58]. The positive test results, about 200,000 cases, represent 80% of all prostate cancers or about 250,000 total cases. This means about 50,000 men, or 8% of the approximately 600,000 men who have negative biopsy results, may not be diagnosed with cancer, despite actually having malignant prostate cancer. In these cases, a "false negative" result is returned and the test will either be repeated or the tumor will go undetected and untreated. Some types of prostate cancer spread

very rapidly. Left untreated, if and when the cancer is finally found, it may be too late to successfully treat, especially if the cancer has spread beyond the prostate.

Needle biopsy is the only conclusive way to confirm a prostate cancer diagnosis. A biopsy needle has a stylet enclosed in a hollow tube called a cannula. The stylet is a long shaft with a sharp tip used to keep the cannula stiff and to cut through tissue. The cannula is 'cocked' during needle insertion to expose the specimen notch as shown in Figure 1(a). Tissue is removed by 'firing' the cannula when the specimen notch has reached the suspected tumor. This moves the cannula over the specimen notch, cutting the tissue that has settled in the notch as shown in Figure 1(b).

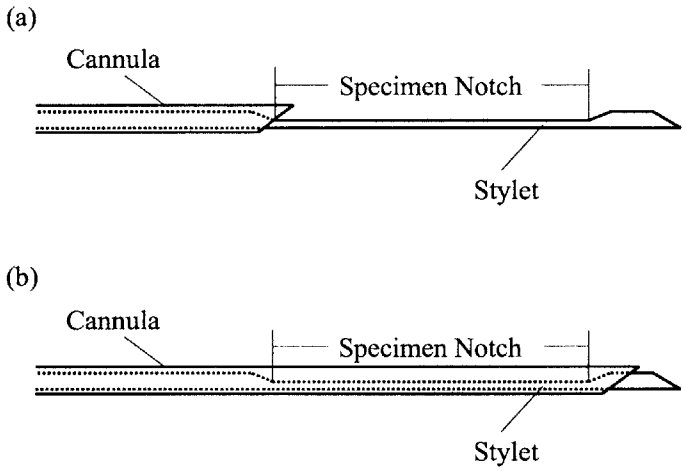

Figure 1: Biopsy needle cocked (a) and fired (b)

This procedure is vital to prostate cancer detection and, hence, treatment. Currently, ultrasound imaging is used to guide a biopsy needle to the prostate. Unfortunately, in too many cases, the biopsy needle misses the tumor because ultrasound images are too low resolution to see small, early stage, tumors. Tumors smaller than 5mm are not detected by ultrasound imaging [20]. Only about 20% of tumors between 5 and 10mm are detected by ultrasound. Even large tumors, on the order of 20 to 25mm, are only detected 79% of the time.

Another problem with this situation is that prostate cancer is a multifocal disease, meaning there are typically many small tumors in the prostate gland. Detecting the large tumors will only eliminate the small tumors if the entire prostate is removed in a procedure called a prostatectomy or if treatment agents are deposited in close proximity, less than 3mm, of the small tumors [62].

Ultrasound images, therefore, cannot be used to detect or treat millimeter size prostate tumors. Even to the untrained eye, it is clear that MR images are far more detailed than ultrasound images. Figure 2 shows ultrasound and MR images of the same prostate. Given the unique imaging capabilities of Magnetic Resonance Imaging (MRI), it is possible to diagnose and treat small, millimeter size tumors that cannot be detected with ultrasound [51,54,62,73].

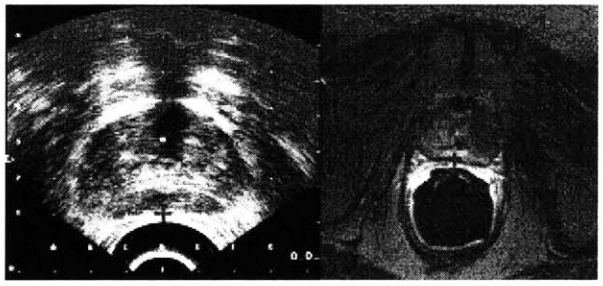

Figure 2: Ultrasound image (left) and MR image (right) of same prostate [24]

There has been substantial research in the development of in-bore MRI manipulation for diagnostic and surgical procedures. Due to the high magnetic fields, conventional robotic actuators, which are typically electromagnetic devices, must be more than 1m from the center of the magnet [5]. This limits the use of conventional actuators, such as DC motors, in these efforts.

In contrast with other technologies, Dielectric Elastomer Actuators (DEAs), a new polymer based actuation technology being developed at MIT, have shown to be MRI compatible [23,64]. DEAs have good performance and low costs, making them very attractive for MRI-compatible robotics [46,64]. Until recently, DEAs were subject to important reliability problems that prevented their commercial use. The reliability of DEAs has been considerably improved

through studies of their failure modes. DEAs can now be used in the design of an MRI compatible needle manipulator for prostate cancer detection and subsequent treatment.

This work develops a needle manipulator with DEAs for use with an MRI scanner. The MR image is used to guide a biopsy or treatment needle to hit a tumor with greater accuracy than current methods. This increased accuracy will help find smaller tumors and allow for earlier, noninvasive treatments. Cancer patients will benefit from earlier diagnosis, more effective treatment, shorter recovery time and reduced risk of side effects (incontinence and impotence). Due to its low cost, this technology has a strong commercial advantage over alternative MRI actuator technologies. Also, the device may be disposable, unlike its expensive counterparts, which require costly, lengthy sterilization.

The challenge is to design a useful system within the constraints of the DEAs. In particular, the DEAs must be used in a binary fashion, which requires many actuators to achieve sufficient precision. DEAs also have very low output forces which limits the overall stiffness of the device. The device is designed such that high stiffness is possible assuming improved manufacturing processes to increase actuator output force.

This MRI-compatible device has the potential to improve or make possible other in-bore MRI procedures. Many treatments and procedures would benefit from the increased visual resolution of MRI, such as breast cancer biopsy and treatment and elastography (palpation) of the breast, prostate, liver and other organs to detect abnormalities.

1.2 Background Literature

Researchers have long sought new ways to improve prostate cancer detection and treatment. This is evidenced by increasing incidence rates, which correlates to the increased use of PSA testing [18], DREs and the regular screening of men under age 65. Most recently, an Early Prostate Cancer Antigen (EPCA-2) test has been shown to more accurately diagnose and

stage prostate cancer than PSA and DRE tests [4]. But, none of these tests confirm prostate cancer. Only needle biopsy and pathology of the removed tissue can confirm malignancy. It cannot, at this time, confirm that a tumor is benign because there are many cases where the tumor is simply missed. Hence, researchers have put much effort into accurately targeting tumors so that biopsy results are accurate and treatment plans are successful.

1.2.1 Prostate Cancer Detection

Both PSA tests and DREs are used for preliminary prostate cancer screening. High PSA scores and/or abnormal DREs indicate the possibility of prostate cancer. If these signs of prostate cancer are found, the only conclusive way to determine if a tumor is malignant is with needle biopsy. During this test, a biopsy needle is inserted through the rectum or the perineum, the area bounded by the legs, anus and scrotum, into the prostate, and a small section of tissue is removed and tested.

This procedure is typically performed by placing an ultrasound probe in the rectum, called TRUS for transrectal ultrasound. The ultrasound image is used to guide the needle to a region as shown in Figure 3. During transrectal needle biopsy, the needle is manually inserted through the rectum. There are some risks associated with this procedure. Most are minor, but include a risk of septic complications [3].

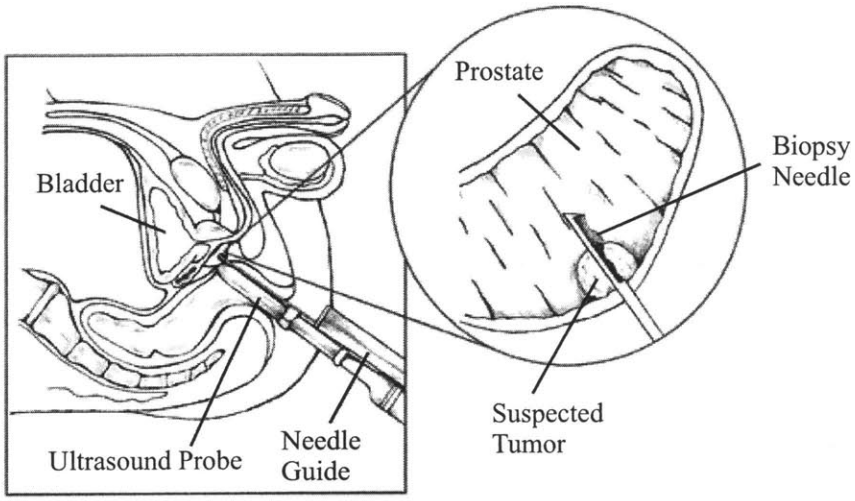

Figure 3: Prostate transrectal biopsy (http://kidney.niddk.nih.gov)

Transperineal biopsy has higher detection rates and lower risks than transrectal biopsy [12]. During transperineal biopsy, a template, which has a grid of holes, is secured against the perineum. A typical template design for transperineal procedures with a transverse slice of an average prostate is shown in Figure 4. The prostate is often divided into several zones, which are superimposed on the template in Figure 4. The peripheral zone (PZ) and the lateral peripheral zone (LPZ) are where most malignancies are found, though some are located in the transition zone (TZ) [45,62].

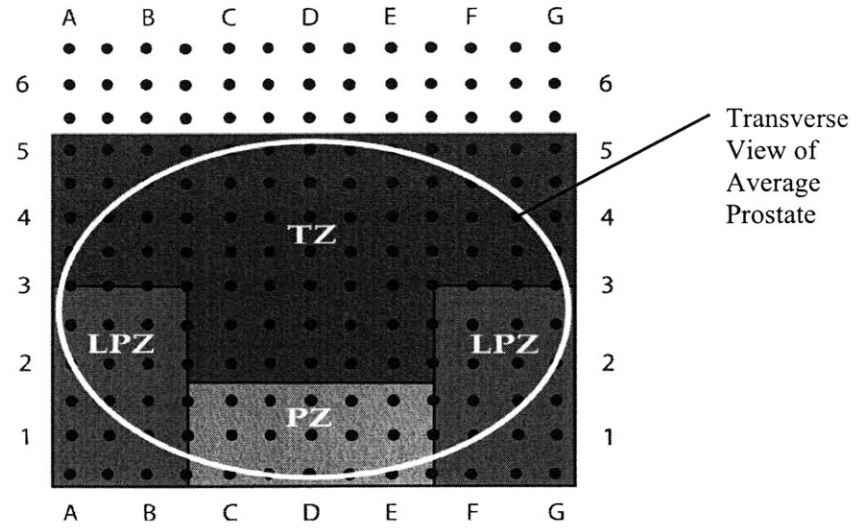

Figure 4: A typical template for transperineal procedures and a cross section of the prostate viewed from the perineum towards the head [45]

A doctor will use the hole that most closely aligns with the region in question. The templates are thick enough to constrain the yaw and pitch of the needle. However, due to the nature of the tissue the needle is traversing, the needle tends to bend. In fact, the needle tip deflects approximately 0.45 to 0.75mm for every 10mm the needle is inserted [65]. In addition, the tissue itself undergoes soft tissue deformation as the needle is inserted.

1.2.2 Prostate Cancer Treatment

If a tumor is detected and determined to be malignant, there are several treatment options. Some men opt to monitor their cancer instead of undergoing treatment, called "watchful waiting." This is typically the case for older men with other health issues and/or in the case of well-contained, very slow growing tumors. For younger men or those with quickly progressing cancer, more proactive measures are taken.

Hormone therapy is a one to two year treatment that reduces the level of testosterone, which, in most cases, slows the growth and/or reduces the size of the tumor. Hormone drug therapy is not a cure as the cancer will usually return and continue to grow once the therapy stops.

Hormone therapy also has many common side effects including hot flashes, osteoporosis, diarrhea, lowered libido and impotence. In severe cases it is often used in conjunction with another treatment.

In very advanced cases of prostate cancer, the cancer may have spread beyond the confines of the prostate gland. In these serious cases, hormone drug therapy is used to reduce the size of the tumor to ensure that it is entirely enclosed by the prostate. Then, a radical prostatectomy is performed. (A radical prostatectomy is not necessarily preceded by hormone therapy.) This is a procedure in which the entire prostate is removed. There are many possible side effects associated with radical prostatectomy. Two common, particularly adverse side effects are incontinence and impotence. More recently, doctors have been performing a nerve-sparing prostatectomy. This has significantly reduced the risk of side effects from the procedure. However, a prostatectomy requires a two to three day hospital stay and several months to fully recover.

The prospect of long treatment duration and recovery time with radical prostatectomy procedures has caused many men to turn to radiation therapy or cryotherapy. External beam radiation therapy is a successful method of prostate cancer treatment with low chance of side effects. However, it requires onsite treatment five days a week for seven weeks, which is a major inconvenience for many prostate cancer patients.

Brachytherapy is a far more common form of radiation therapy because it is an outpatient procedure, as is cryotherapy. Both have a recovery time of only a few days. During brachytherapy and cryotherapy, similar to needle biopsy, a needle is inserted into the tumor in the prostate, typically using an ultrasound image for guidance. In brachytherapy, the needle deposits small radioactive pellets in the tumorous region. Cryotherapy uses very low temperatures to "freeze" a tumor. Though the last step of the procedures is very different, depositing radiation pellets versus cryogenic agents, the needle delivery method is the same.

In this study, prostate cancer needle biopsy, brachytherapy and cryotherapy applications are considered. All can be performed either by inserting the needle through the rectum or through the perineum. A transperineal approach shown in Figure 5 has a lower risk of hitting vital structures than a transrectal approach, Figure 6. In a transperineal approach, there is a lower risk of infection and no need for antibiotics because the insertion happens in a clean environment. And, detection rates are higher with a transperineal approach.

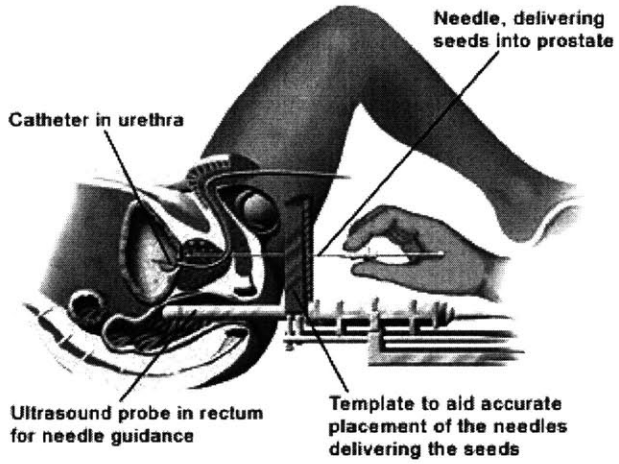

Figure 5: Prostate cancer transperineal brachytherapy treatment (www.prostatecancercentre.co.uk)

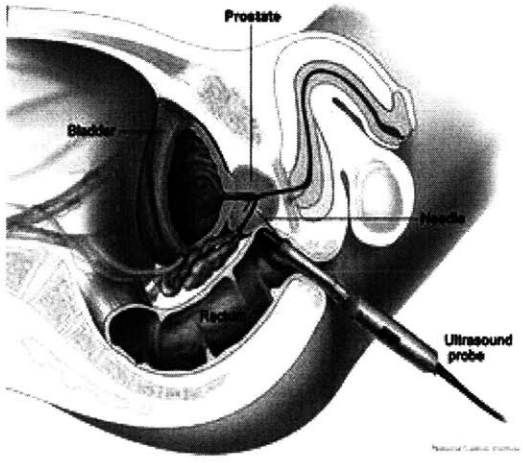

Figure 6: Prostate cancer transrectal brachytherapy treatment (www.cancer.gov)

Transperineal brachytherapy is growing in popularity over other treatment options because of a significantly smaller chance of incontinence and impotence, quick treatment and recovery and high success rates [39]. As brachytherapy becomes the method of choice, the procedure must become more reliable. Early detection through accurate biopsy needle placement is equally crucial to treating prostate cancer. To increase prostate cancer survival rates, it follows that needle placement methods must be improved.

1.2.3 Needle Placement

There are several inherent problems with the current transperineal ultrasound guided approach:

- The ultrasound image is not sufficient to detect small tumors.
- The template limits the entrance location at the perineum.
- The template eliminates the possibility to adjust for needle deflection and tissue deformation.

There has been significant work in needle trajectory planning to account for needle deflection and tissue deformation before beginning procedures [10,40]. In addition, efforts have been made using this information to train doctors to correct for needle deflection during surgery [1,26,72]. However, having a template significantly reduces the ability to implement successful planning. Doctors are essentially trying to hit a suspected tumor they cannot see with a needle they cannot control.

Several methods have been developed for real time control of needle insertion. A modified biopsy needle uses a bent stylet within a straight cannula as shown in Figure 7 [43]. The needle is "steered" by varying the length of the stylet exposed to tissue. This method has been successfully automated using conventional extension and rotation motors.

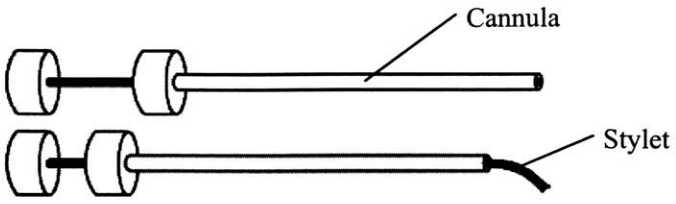

Figure 7: Steerable needle [43]

A "tapping" method is used to decrease the rotation and deformation of the prostate [32]. This technique inserts a single needle just beneath the skin of the perineum. This point is used as a rotation point to modify the final location of the needle (Figure 8). It may be possible to slightly change the path of the needle when it is further inside the tissue without causing too much damage to the tissue.

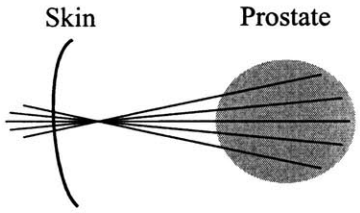

Figure 8: Tapping method [32]

The tapping method would result in conical implantation of brachytherapy pellets. The feasibility of such an approach has been studied in patients who had previously been treated with a rectangular template [16]. Results show that the dosage achieved using a conical approach is comparable to using a rectangular template and, it is even possible to reduce the total number of required seeds by optimizing the seed spacing.

Robotic needle manipulation, using visual ultrasound feedback control, is another area of research focused on improving prostate cancer detection and treatment [50,71]. One robotic manipulator has 6 degrees of freedom using stepper motors and a transrectal ultrasound image to guide a needle to the prostate [50]. This study concluded that robotic needle insertion is more accurate than manual insertion because unsteady motions are eliminated. A manipulator with 9

degrees of freedom, of which 5 are manual and 4 are motors, achieves errors of less than 2.5mm [71]. This particular work uses software to determine and adjust for needle deflection.

These low errors represent the manipulator repeatability and do not reflect the poor accuracy of ultrasound in differentiating prostate cancers. Recall from Section 1.1 that tumors smaller than 5mm cannot be identified at all [20]. Low errors are also only achievable by using stiff needles, which is not possible in an MRI. MR compatible needles cannot be steel like regular biopsy needles; they are typically a titanium alloy, and tend to be flexible [62].

However, despite all these efforts, inadequate visualization of the tumor hinders any true breakthroughs in this area. The highly detailed images produced by MRI provide the information necessary to accurately hit targets, even very small, millimeter size tumors. In recent years, there has been an increase in research leading to MRI guided prostate interventions [19].

One class of MRI manipulation is intended for use with an open-bore MRI. An open-bore MRI, instead of having a closed tube, has two magnetic coils. This provides a space for a physician to access the patient. A surgical assist robot with 6 degrees of freedom uses remote conventional actuators as well as an ultrasonic motor for linear actuation [29,30]. This manipulator is very large because it is primarily remotely actuated. It would not be suitable for use in a closed-bore MRI scanner.

Many researchers have used piezoelectric motors in manipulator designs for use in MRI systems [6,7,11,33,37,41]. For example, a surgical assist robot has been tested successfully in an experimental 0.7-Tesla open-bore MRI [6]. However, there have been reports of image distortion when using piezoelectric motors in the bore of a closed-bore MRI [67]. Ideally, doctors would like to be able to use a closed-bore image, which has a much higher field strength, in the 3 Tesla range. Open-bore MRIs have significantly lower precision than closed-bore MRIs. Their images are not detailed enough or suitable for accurately treating a tumor on the order of 5mm [51]. Moreover, open-bore MRI machines are generally research machines and are not widely

available. Even if it were possible to configure piezoelectric motors such that they could be used in a closed-bore without distorting the MR image, these actuators are slow, complex and expensive.

Other manipulators using pneumatics have had limited success in conjunction with closed MRI [9,14,55,56,57,61]. The main drawbacks to this approach are control issues due to the imprecision and compliance of pneumatics. Pneumatic stepper motors have been designed to eliminate these effects [57]. The valves required in pneumatic actuation are often driven by solenoids, which cannot be used in an MRI. Some solutions use long plastic tubes in order to remotely actuate the valves, but this may lead to slow responses [57,61]. Another replaces the solenoids with piezoelectric actuators [14]. This, again, poses the issue of possible image distortion [67].

Researchers have been successful using other remotely actuated manipulators. One configuration is a device that is remotely and manually actuated by a doctor [13,31]. Its MRI compatibility is achieved by eliminating automatic actuation. This device uses a transrectal approach, which requires antibiotics and has a higher risk of hitting vital organs than a transperineal approach. Also, it is only intended to perform needle biopsy at this time. Other researchers have used conventional actuators, but placed them far from the bore of the MRI [17,63]. This approach is impractical because it requires a very large, complicated device.

1.2.4 Dielectric Elastomer Actuators

DEAs consist of a thin dielectric elastomer film sandwiched between two compliant electrodes (Figure 9) [27]. When a high voltage is applied across the electrodes, the dielectric film is squeezed by electrostatic forces. This causes thinning of the film and an expansion of its planar area. Constraining the motion of the film with mobile frames results in useful output motion and force [27].

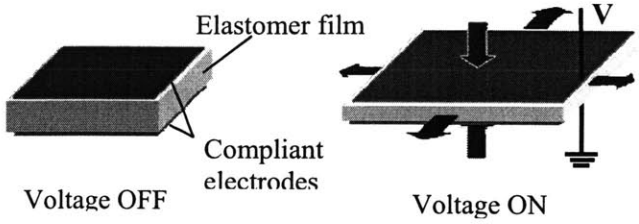

Figure 9: DEA operating principle [27]

Practical DEAs can have large linear extensions of more than 100% (Figure 10). Under laboratory conditions, these actuators have shown substantial energy densities (actuator mechanical work per unit mass of actuator), significantly exceeding those of conventional technologies such as electromagnets [28,69]. Further, they are lightweight, simple, and low cost compared to conventional actuators.

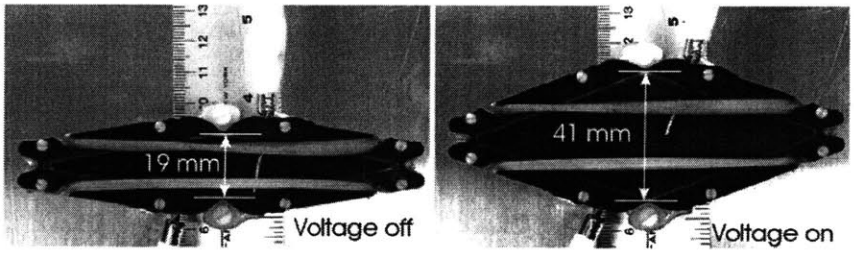

Figure 10: Unactuated (left) and actuated (right) DEA [46]

A key feature of the DEAs developed at MIT is their MRI compatibility due to their all polymer construction [23,64]. However, until recently, DEAs have experienced reliability problems leading to erratic and unexplained failures. Consequently, marketable products using these actuators have yet to be realized. Results of an intensive study of how and why DEAs fail explain the failure modes and the conditions leading to failure [48]. An important conclusion is that DEAs show significantly better reliability when used intermittently at high speeds. At high speeds, viscous forces build up in the film and resist an unstable failure mode called pull-in.

As a result of these studies, DEAs now have the potential to be reliable, simple, low cost, effective actuators, which can be used within the bore of an MRI. Hence, they are used in this work in the design of a needle manipulator to improve prostate cancer diagnosis and treatment.

Any mechatronic device that uses DEAs must actuate them intermittently at high speeds to maximize performance and minimize reliability issues. To do so, devices must be designed according to the binary actuation paradigm where actuators are used to flip between one of two discrete states [44,49,52]. Figure 11(a) shows the basic concept of bistable actuation. When DEA 1 is turned on, the bistable element flips to its other stable position. When DEA 2 is subsequently actuated, the bistable element returns to its original position.

Bistable actuation is beneficial to MRI applications because the DEAs are powered off during imaging, further reducing the possibility of image distortion. Also, systems design and control is greatly simplified since low-level feedback control is virtually eliminated, along with the associated sensors, wiring, and electronics [60]. A bistable actuator can be made by using two DEAs that flip a bistable element between its stable positions as shown in Figure 11(b).

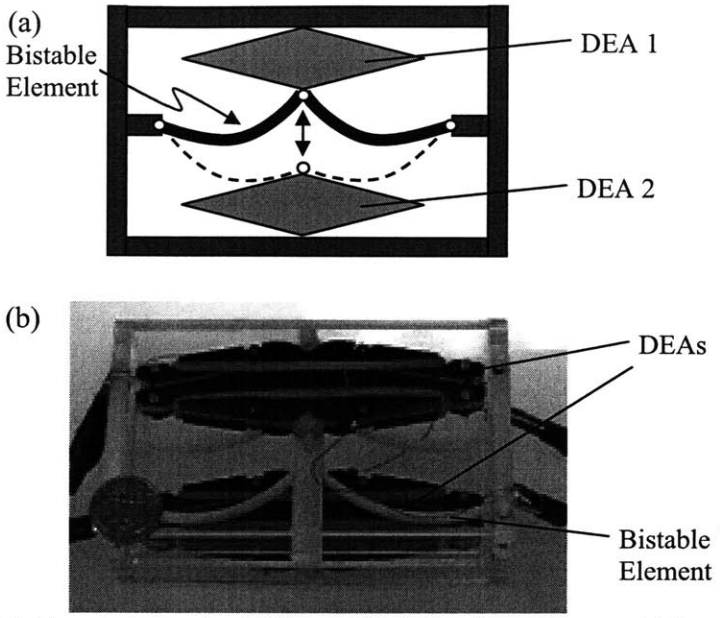

Figure 11: Bistable actuator using DEAs and bistable element concept (a) and prototype (b) [49]

A mechatronic system using bistable actuators can only reach a finite set of discrete points. In order to obtain a fine resolution that can compete with continuous systems, a needle manipulator must have many degrees of freedom. Studies suggest that most practical tasks will require between 10 to 100 degrees of freedom (DOF) to provide sufficient resolution and that the associated computing requirements for solving their inverse kinematics are reasonable [34,35]. A possible binary manipulator using a serial chain of DEAs was developed in preliminary work, see Figure 12 [46]. Such large serial binary chain robotic systems have been considered, but they offer low resistance to outside forces, which makes them unable to withstand the forces imposed during needle insertion [46,49,68,70].

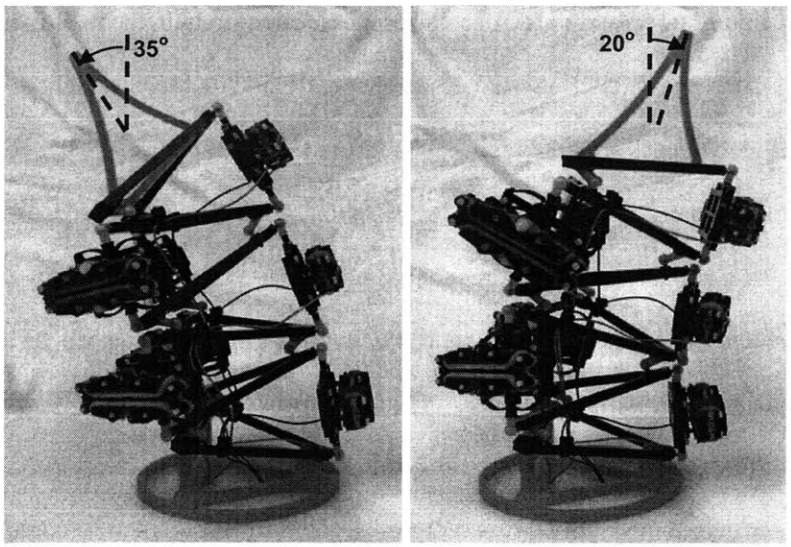

Figure 12: 7 DOF binary manipulator prototype

The approach taken in this research applies the new MRI compatible technology, polymer actuation. Dielectric elastomer actuators can be placed inside the bore of an MRI without affecting the image and without any effects on the actuators, not requiring any complicated transmissions. This results in a simple design and a potentially low cost manipulator for real time vision guided control using MR imaging.

1.3 Approach and Thesis Overview

As previously discussed, DEAs must be used in a binary manner [46,48]. Unlike conventional systems that use only one continuous actuator per degree of freedom, bistable systems require many actuators per degree of freedom to obtain high precision. This results in an over constrained system. Compliance is used to accommodate for this over constraint in a method called elastic averaging [53]. The natural compliance of the bistable actuators and any added system compliance are used to mediate between the bistable actuators to reach a position with high precision.

Device size, force and workspace size and accuracy requirements are established for a needle manipulator in conjunction with researchers at Harvard Medical School's Brigham and Women's Hospital and are presented in Chapter 2. A system design using MRI compatible DEAs is developed in Chapter 3. The system uses DEAs intermittently at high speeds to avoid failure modes [48]. Redundant actuators are connected using compliant elements to result in an elastically averaged system. Two separate planes of elastically averaged bistable DEAs are combined to generate the workspace necessary at the prostate.

The stiffness and accuracy of the system are developed in Section 3.3. Appropriate parameters are determined for three designs: a clinical prototype, a complete laboratory prototype, Beta, and a simplified laboratory prototype, Alpha. The laboratory prototypes' stiffnesses are constrained by the low force current actuators generate. The clinical prototype design assumes adequate forces can be generated using automated manufacturing procedures.

The design is analyzed in Sections 4.2 and 4.3 using an analytical mathematical model implemented in MATLAB®. These calculations show that the device would provide an adequate workspace for the prostate cancer application. They also suggest that by making adjustments to design parameters, the manipulator could be modified for use in other real-time MRI guided surgeries.

A mockup of the manipulator using solenoids instead of DEAs is discussed in Section 4.5.1 and experimental results are compared to expected results. These tests demonstrated repeatability and showed good correlation to mathematical workspace predictions.

The construction of a laboratory prototype Alpha is discussed in Section 4.5.2. MRI testing shows compatibility is maintained.

1.4 Results

The method to achieve the necessary workspace has been developed, analyzed, and tested and shown to be effective. The needle insertion method is the next key step in the development of this manipulator. This mechanism must be able to produce up to 15N of force and achieve high precision in order to ensure that the manipulator accurately hits suspected regions in the prostate and avoids hitting any vital structures. Following development of this system, phantom testing must be performed.

The design parameters of this manipulator can be modified to accommodate other precise needle placement procedures. By modifying system parameters the workspace shape, size and accuracy as well as the overall system stiffness can be significantly altered. Other potential applications of precise needle placement using MR imaging include cancer detection and treatment, particularly breast cancer [15,33,66].

1.5 Summary

MR imaging has the potential to greatly improve prostate cancer detection and treatment. DEAs are MRI compatible and a good alternative actuation technology for this application. This thesis develops the requirements, design and analysis of an MRI compatible needle manipulator using DEAs.

CHAPTER

2

REQUIREMENTS FOR A NEEDLE MANIPULATOR FOR PROSTATE CANCER DETECTION AND TREATMENT

2.1 Introduction

Specifications for an MRI compatible robotic needle manipulator are developed with researchers at Harvard Medical School's Brigham and Women's Hospital. The device must be MRI compatible, small enough to fit between a patient's legs while he is inside the bore of an MRI, produce a workspace comparable to current approaches and be able to resist forces during insertion.

2.2 Function of Needle Manipulator

The device developed in this work is intended primarily for use in prostate cancer detection and treatment, specifically for biopsy, brachytherapy and cryotherapy procedures. A transperineal approach is used because it has higher detection rates and a lower chance of infection than a transrectal approach. The objective of this research was to develop an MRI compatible manipulator that will use a real time MR image to accurately guide a needle to a suspected, or confirmed in the case of treatment, tumor.

2.3 Specifications

2.3.1 Size

The device must be MRI compatible and able to fit between the patient's legs while inside the bore of the MRI, see Figure 13. The bore of a typical MRI is 550mm in diameter [8]. There is a cradle that the patient lies on, which reduces the diameter to about 450mm. The patient's legs are propped up to provide access to the perineum. This leaves a small space for the device to reside. This requires that the device be no larger than a 200mm diameter cylinder, 500mm deep.

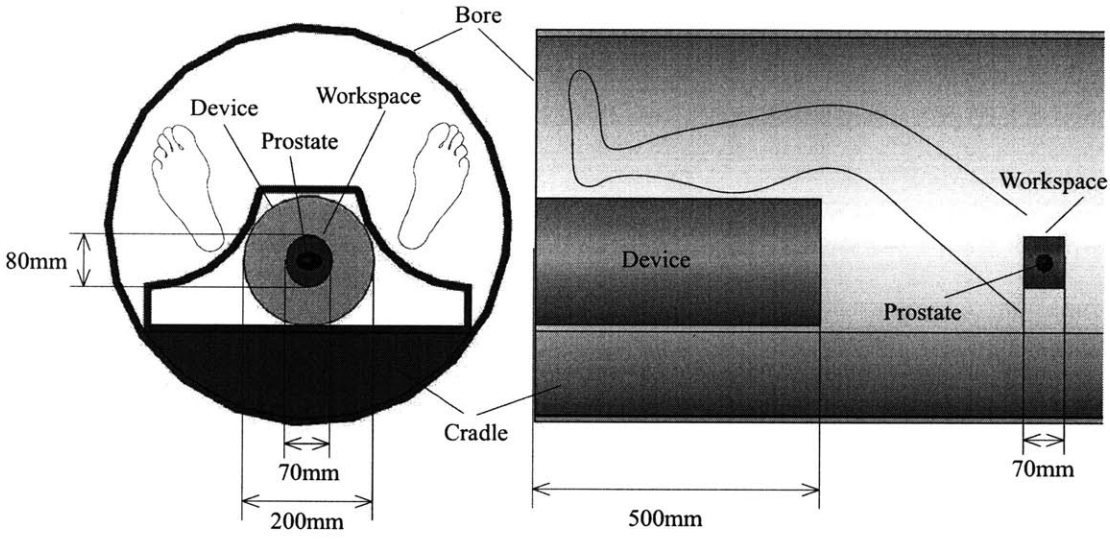

Figure 13: Device size and workspace requirements

2.3.2 Position Precision and Workspace

Under the control of a doctor using a real-time MR image, the proposed device is required to reach a target (a tumor) in the prostate at point (x_d, y_d, z_d) by penetrating the perineum as shown in Figure 14. The average prostate is located 60 to 80mm from the perineum, and the size of the average prostate is 30 to 50mm in the z-direction [16]. The needle must be able to travel between 60 and 130mm in the z-direction. The manipulator must have an accuracy of

±5mm in order to improve on current technology by enabling the detection and destruction of tumors in the early stage of development.

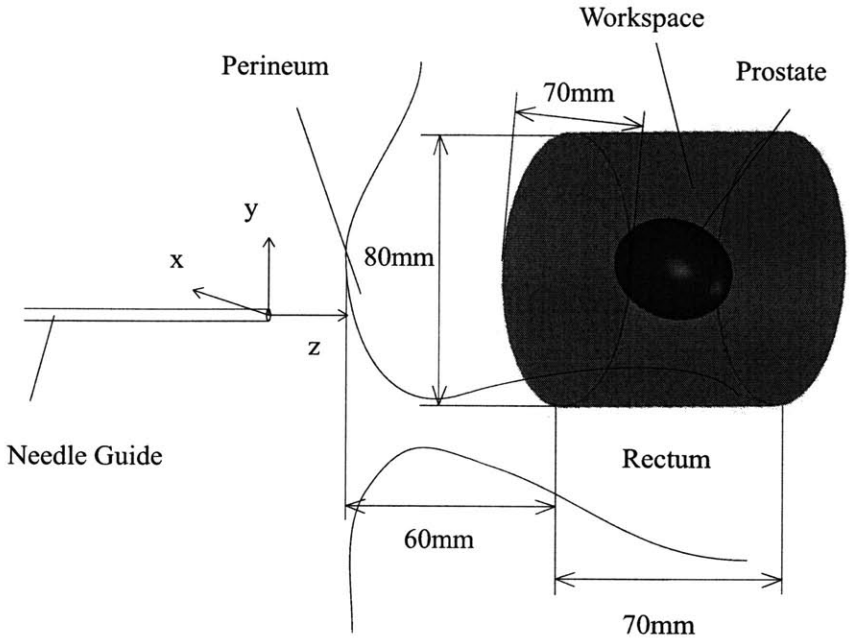

Figure 14: Needle path and workspace requirements

The required workspace is roughly an elliptic cylinder with a major axis of 80mm and a minor axis of 70mm, 70mm in the z-direction, as shown in Figure 13 and Figure 14. This workspace is larger than the average normal prostate, but is necessary to accommodate the frequently enlarged prostates of cancer patients as well as position differences from patient to patient.

2.3.3 Force

To establish the forces on the needle that the manipulator must withstand, beef muscle tissue tests were performed. Beef muscle has similar properties to those of the flesh between the perineum and the prostate [50,51]. Figure 15 and Figure 16 show representative results of the

insertion force and the resultant transverse forces of inserting a needle 20mm into beef muscle. It is beneficial to use a trihedral needle instead of a beveled needle (Figure 17): forces are lower and trihedral needles often take better biopsy samples than beveled needles [62]. Extrapolating the forces imposed on the trihedral needle from 20mm to 110mm, a representative distance of tissue traversed in prostate cancer interventions, the maximum expected force of insertion is ~8.25N and the maximum transverse force is ~0.5N.

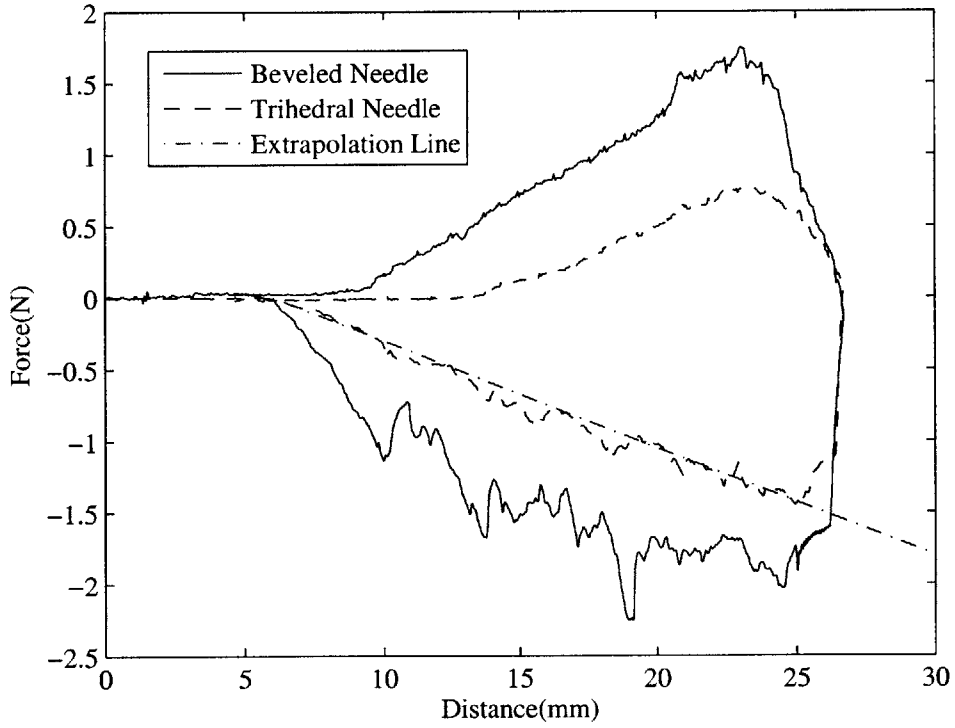

Figure 15: Force to insert needle 20mm into beef muscle

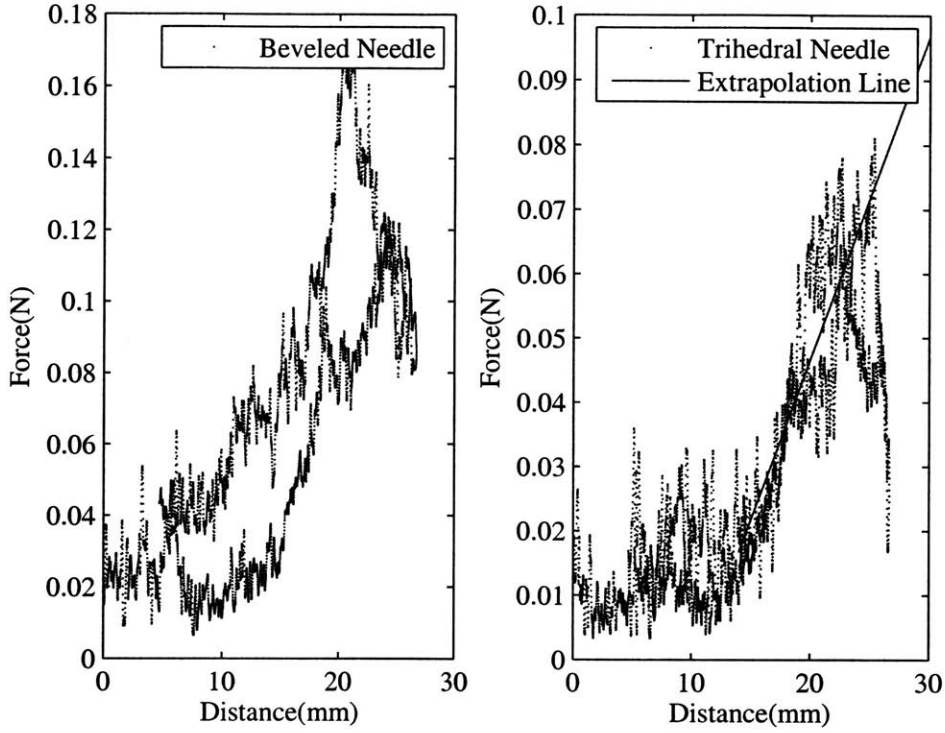

Figure 16: Resultant transverse force to insert needle 20mm into beef muscle

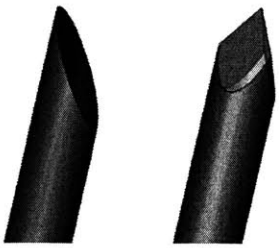

Figure 17: Beveled (left) and trihedral (right) needle tips

The literature shows that there is a peak insertion force when penetrating human skin, as shown in Figure 18 [50]. During these brachythrapy procedures, there is a maximum insertion force if 14N, which then has a local maximum of 8N. In Figure 19, the transverse force fluctuates around 0.7N. These numbers were obtained during hand held needle insertion. In this study, both hand held insertion and robotic insertion were demonstrated on beef wrapped in chicken skin in an attempt to simulate the perineum and prostate [50]. During robotic needle

insertion, results show significantly lower forces that hand held needle insertion. The insertion force has a peak 1.5 times higher by hand than by robot. The transverse force exhibits a difference of a factor of 3. These are due to differences in velocity and acceleration during insertion. Changes in velocity during manual insertion allowed the tissue to settle around the needle, resulting in higher forces than during robotic insertion.

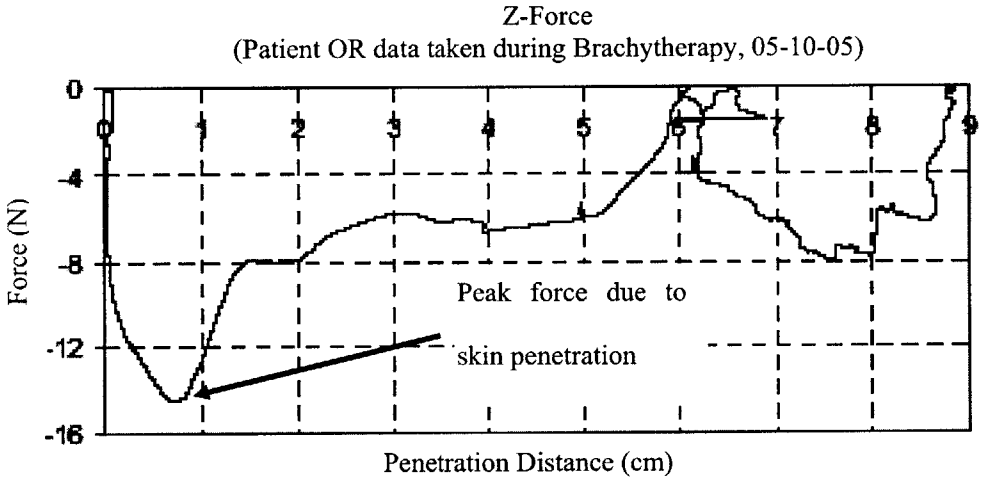

Figure 18: Insertion forces during brachytherapy procedure [50]

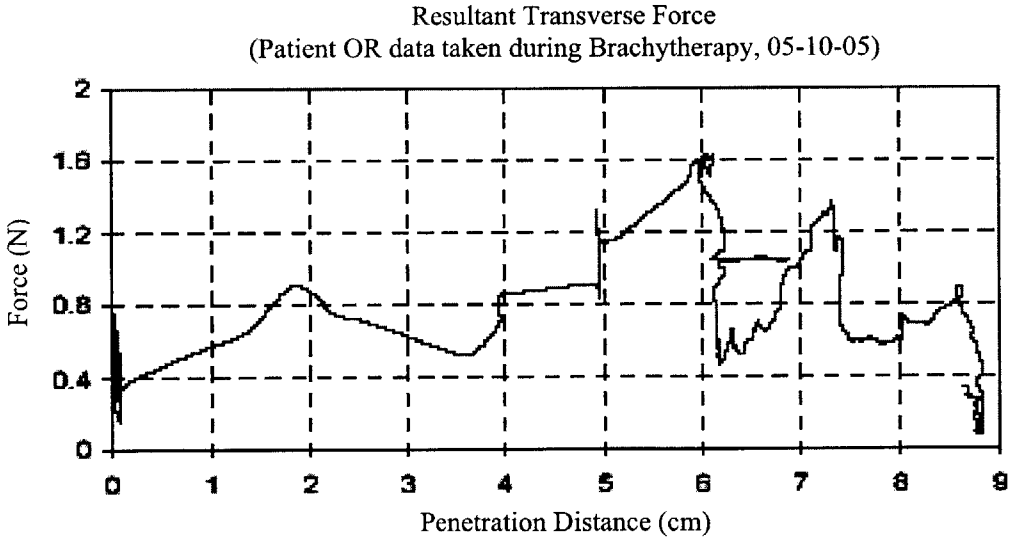

Figure 19: Resultant transverse force during brachytherapy procedure [50]

Experimental results and those from the literature are considered to reach a reasonable set of specifications with researchers at Brigham and Women's Hospital [8,25,50]. The maximum penetration force required for the manipulator is set at 15N in the direction of needle travel to ensure penetration of the skin is possible. The maximum transverse force the needle must resist is 1.6N.

2.4 Summary

Table 1 shows the requirements for an MR compatible needle manipulator for prostate cancer detection and treatment. Two prototype designs are considered: Alpha and Beta. The Alpha prototype is a simplified version of the Beta prototype designed for manufacture by hand, in a limited time frame. Actual laboratory prototype Alpha values and projected prototype Beta adherence to requirements are also displayed in Table 1. Chapter 3 explores the development and design of the prototypes and the clinical device.

Table 1: Requirements, laboratory prototype specifications and projected clinical device specifications

		Clinical Requirements	Prototype Alpha	Prototype Beta
Size	Diameter	200mm	400mm	400mm
	Depth	500mm	130mm	450mm
Workspace	Diameter	80 x 70 mm	8mm x 8mm	80 x 70 mm
	Depth	70mm	Not Applicable	70mm
Force	Transverse	1.6N	0.45N	0.15N
	Penetration	15N	Not Applicable	To Be Determined

CHAPTER

3

THE DESIGN OF AN MRI COMPATIBLE NEEDLE MANIPULATOR USING DEAS

3.1 Introduction

Dielectric elastomer actuation is used in the design of an MRI compatible needle manipulator. In order to avoid reliability issues, the DEAs are only used in a bistable manner. This limitation leads to a design using elastic averaging to mediate between actuation and center point locations. To achieve a full workspace at the prostate, two planes of elastically averaged DEAs are utilized with a needle running through the center point of each plane.

3.2 System Design

The basic design concept using these principles is shown in Figure 20. Binary robotics, elastic averaging and parallel mechanisms are used to achieve high precision. The needle is oriented by the motion of the center point of two parallel planes. Each plane has six bistable actuator modules connected to a center point by springs. The springs are used to mediate between the modules. Different center point locations, and hence needle orientations, are achieved by actuating different bistable actuator module combinations. The workspace at the prostate is achieved by advancing the needle through the planes, towards the prostate. This mechanism has not yet been developed and is considered continuous in the following analysis.

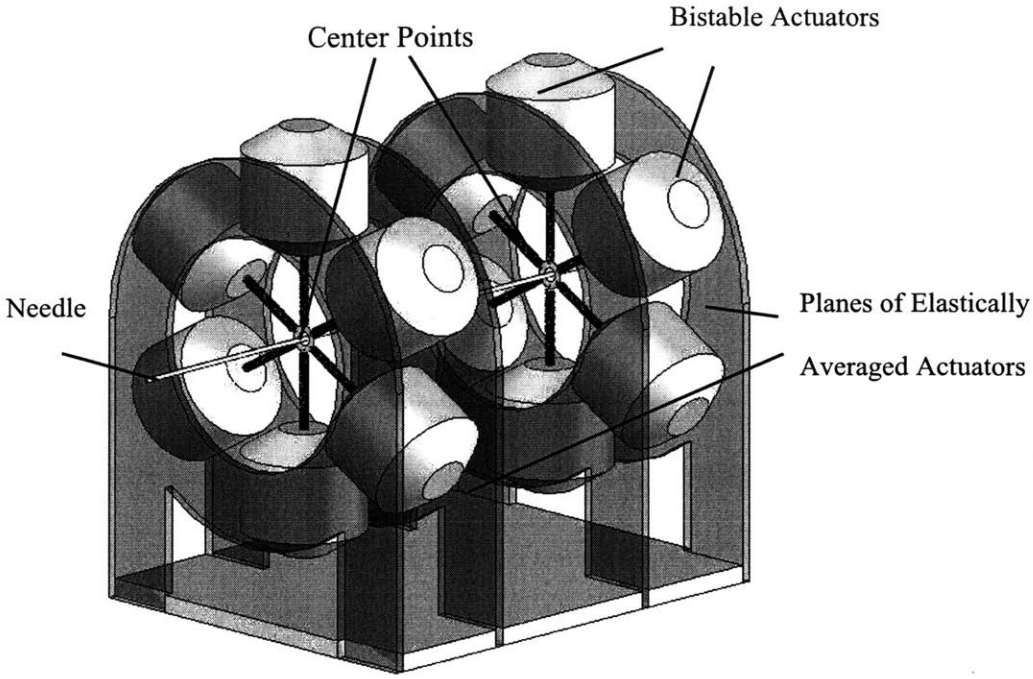

Figure 20: System design

3.2.1 Theory of Operation

The robotic needle manipulator clinical system has been developed to adhere to size, force and workspace constraints for prostate cancer detection and treatment. At the start of a biopsy or treatment procedure, an MR image will be taken of the pelvic region. This will be used for preoperative planning and to properly align the device such that the center of the individual's prostate will be in line with the origin of the device. The device will then be secured to the table of the bore between the patient's legs.

The device will align the needle such that the projected path of the needle is in line with the tumor. This method allows for adjustment of the needle if necessitated by needle deflection and/or tissue deformation while the patient is in the bore of the MRI. MR images will be taken throughout the needle positioning and insertion to ensure the tumor is accurately targeted and vital structures are avoided. "False negative" results will be minimized by vision guidance. This

will allow the doctor to conclusively diagnose a tumor and to more successfully treat a malignant tumor.

3.2.2 Design Concept

The manipulator uses the concept of "elastic averaging" [53]. In this design, several bistable actuators are connected to a center point by springs as shown in Figure 21. Each bistable actuator can independently be activated to a predetermined extension. The springs deform to place the center point in an equilibrium position between the bistable actuators. Each reachable center point location is coupled with a certain configuration of the bistable actuators. The main advantage of an elastically averaged manipulator over serial chains is that many redundant actuators can be used which greatly improves system stiffness.

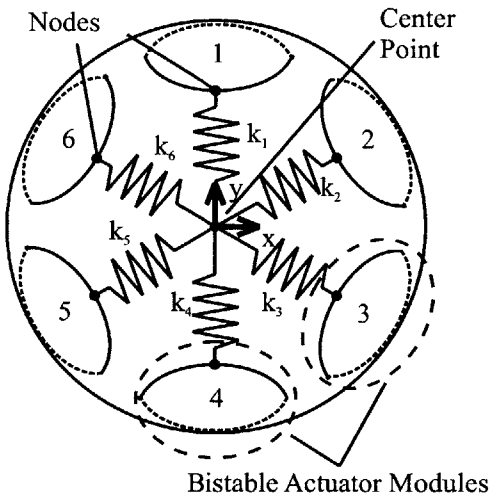

Figure 21: Elastic averaging

The full workspace of the system is produced by using two parallel planes of elastically averaged bistable actuators as depicted in Figure 22. The surgical needle runs through a tube held at the nominal center of each actuator plane advancing from Plane 1, p_1, through Plane 2, p_2, to the target. This results in a conical space envelope, which has been shown to be comparable to rectangle template methods [16].

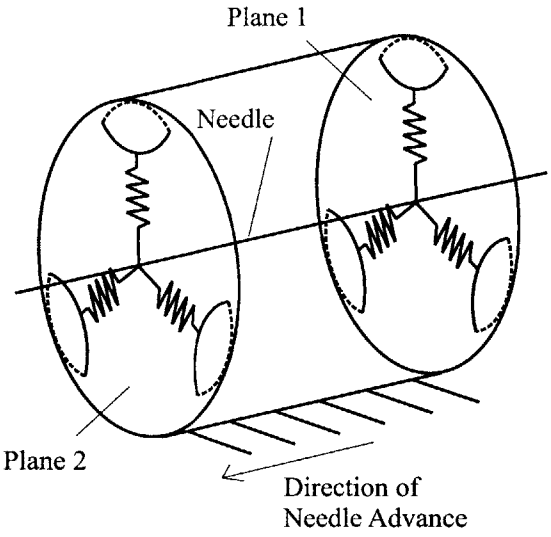

Figure 22: Parallel planes

An elliptic workspace at a given insertion depth is achieved by choosing appropriate spring stiffnesses. The stiffnesses are also set such that the possible end point locations are more plentiful in the peripheral zone of the prostate.

3.3 Theoretical Stiffness and System Accuracy

Each plane of the system has a set of compliant elements and nodes, which are inputs, see Figure 23 [38,59]. The compliant elements are modeled as ideal springs. The nodes have binary positions imposed by the bistable actuators, each composed of an antagonistic pair of actuators that flip a bistable element to one of two known positions, as discussed in Section 1.2.4.

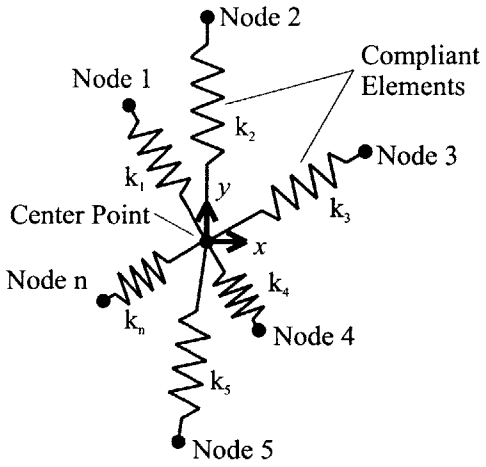

Figure 23: System of nodes attached to the output of the bistable actuators.

The deformation of the springs and internal forces due to the external forces at the center point and the motion of nodes *1* through *n* at the bistable assemblies are shown in Figure 24(a) and Figure 24(b) respectively where:

k_i = stiffness of *i*th spring

and the inputs:

$\underline{\delta_i}$ = stroke of *i*th actuator along axis of *i*th undeformed spring

$\underline{f_{ext}}$ = external force vector at center point

$\underline{W}$ = weight vector at center point

result in the outputs:

$\underline{x}$ = vector displacement of center point

$\underline{F_i}$ = internal force due to *i*th actuator module along axis of *i*th deformed spring

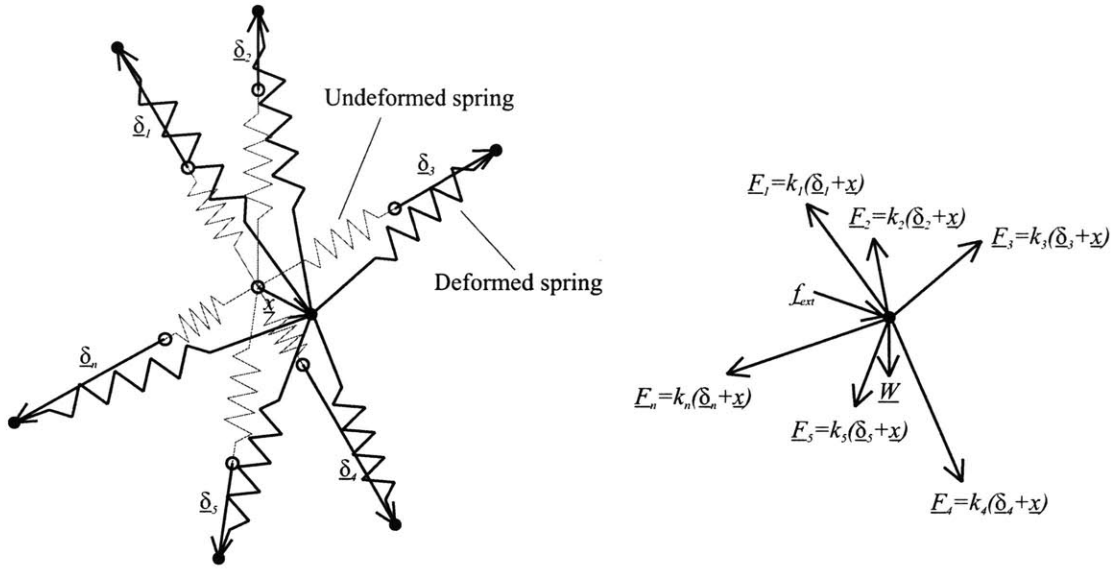

(a) Displacements (b) Forces

Figure 24: Node and center point displacements (a) and free body diagram (b)

For static equilibrium, the sum of the forces at the center point must equal zero:

$$\sum forces = \sum_i \underline{F}_i + \underline{f}_{ext} + \underline{W} = \underline{0} \tag{3.1}$$

And the internal force due to the *i*th actuator module is:

$$\underline{F}_i = k_i(\underline{\delta}_i - \underline{x}) \tag{3.2}$$

These equations are solved iteratively for $\underline{x}$ using the Nelder-Mead method in MATLAB® (fminsearch). The direction of each vector $\underline{\delta}_i$ is known and is determined by the configuration of the each bistable actuator module (see Figure 21). Then the sum of forces is:

$$\sum_i \begin{Bmatrix} F_{ix} \\ F_{iy} \end{Bmatrix} = \sum_i \begin{Bmatrix} k_i\left(\|\underline{\delta}_i\|\cos\varphi_i - \|\underline{x}\|\cos\theta_x\right) + \|\underline{f}_{ext}\|\cos\theta_f \\ k_i\left(\|\underline{\delta}_i\|\sin\varphi_i - \|\underline{x}\|\sin\theta_x\right) + \|\underline{f}_{ext}\|\sin\theta_f - \|\underline{W}\| \end{Bmatrix} = \begin{Bmatrix} 0 \\ 0 \end{Bmatrix} \tag{3.3}$$

where φ_i is the angle of the vectors $\underline{\delta}_i$, θ_x is the angle of the displacement of the center point and θ_f is the angle of the external force. The magnitude of the strokes, $\|\underline{\delta}_i\|$, is the displacement imposed by the actuators on the springs.

This method is used to solve for the workspace of each plane of the system independently, where there are n actuator modules per plane and m end effector locations. In order to calculate the exact locations, (x_{dm}, y_{dm}, z_{dm}), of the end effector of the manipulator, the needle tip, the following equation is used:

$$\underline{X}_d = \underline{X}_1 + \frac{z_{dm}}{p}(\underline{X}_2 - \underline{X}_1) \tag{3.4}$$

where $\underline{X}_1$ and $\underline{X}_2$ are the workspace of the two parallel planes, each with 2^n end effector coordinates, (x_{in}, y_{in}, z_i), in plane i, p is the parallel distance between the planes and the origin, $(0,0,0)$, is the center point of p_1 before any perturbation as shown in Figure 25. Since, the origin is set at the center of p_1, z_1 is 0 and z_2 is p.

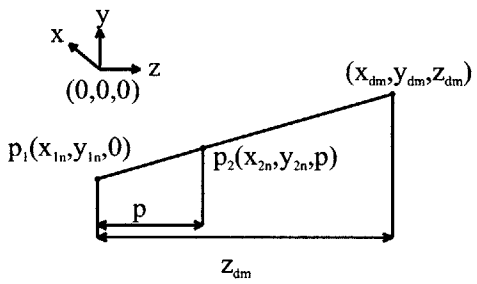

Figure 25: Workspace at p_1, p_2 and end effector

The workspace, $\underline{X}_d$ is comprised of 2^N points, where $N = 2n$ is the total number of bistable actuator modules in the system. The accuracy of the system can be approximately defined as:

$$accuracy = \pm\frac{l}{2} \tag{3.5}$$

where l is the average distance between points:

$$l = \sqrt[r]{\frac{W}{2^N}} \tag{3.6}$$

and W is the size of the workspace. If discrete actuation is used for insertion, then W must be the volume of the required workspace and r must be 3. However, since the method for needle advancement has not yet been developed, it is assumed that the workspace is continuous along the axis of the needle. For this case, W is the area at a slice of the required workspace, a 70 x 80mm ellipse, and r is 2. Given a required accuracy and area, the number of actuator modules necessary can be determined. Appropriate stiffness is dependent on the force and accuracy requirements of a system as well as the configuration of the actuator modules.

As actuator modules are added to the device, the overall stiffness increases. The stiffness varies depending on the exact configuration of the system. However, assuming small displacements, an equivalent spring constant can be calculated for the manipulator.

The planes can be represented as they are in Figure 26. Given this configuration, an external force, (f_x,f_y), in the plane results in a displacement, (d_x,d_y), of the center point. Assuming small displacements:

$$\begin{bmatrix} f_x \\ f_y \end{bmatrix} = \begin{bmatrix} \frac{\sqrt{3}}{2}(k_2 + k_3 + k_5 + k_6) & 0 \\ 0 & k_1 + k_4 + \frac{1}{2}(k_2 + k_3 + k_5 + k_6) \end{bmatrix} \begin{bmatrix} d_x \\ d_y \end{bmatrix} \tag{3.7}$$

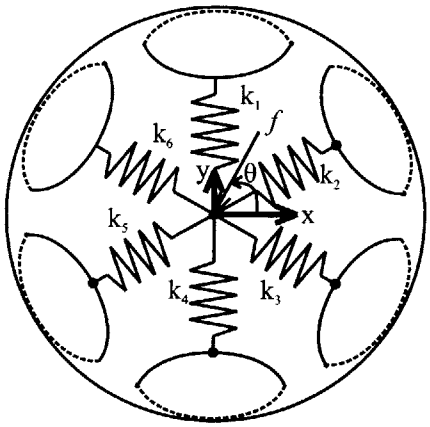

Figure 26: Force applied at center point

K_x and K_y, then, are defined as:

$$\begin{bmatrix} f_x \\ f_y \end{bmatrix} = \begin{bmatrix} K_x & 0 \\ 0 & K_y \end{bmatrix} \begin{bmatrix} d_x \\ d_y \end{bmatrix} \tag{3.8}$$

Using Hooke's Law, the equivalent stiffness in each plane can be defined as:

$$k_{eq,plane} = \sqrt{K_x^2 \cos^2\theta + K_y^2 \sin^2\theta} \tag{3.9}$$

So, $k_{eq,plane}$ is dependent on the angle, θ, of the force. The equivalent stiffness of the entire system can be defined in several ways. The equivalent stiffness at the center of the two planes is:

$$K_{eq,cen} = \frac{4k_{eq1}k_{eq2}}{k_{eq1} + k_{eq2}} \tag{3.10}$$

More importantly, the equivalent stiffness at a distance, ζ, from the p_2, neglecting the stiffness of the needle itself is:

$$K_{eq,tip} = \frac{k_{eq1}k_{eq2}p^2}{k_{eq1}(p+\zeta)^2 + k_{eq2}\zeta^2} \tag{3.11}$$

where p is the distance between the planes and ζ is a distance from p_2 towards the prostate as shown in Figure 27. Unless otherwise specified, the equivalent stiffness will refer to this stiffness where ζ is the distance from p_2 to the perineum.

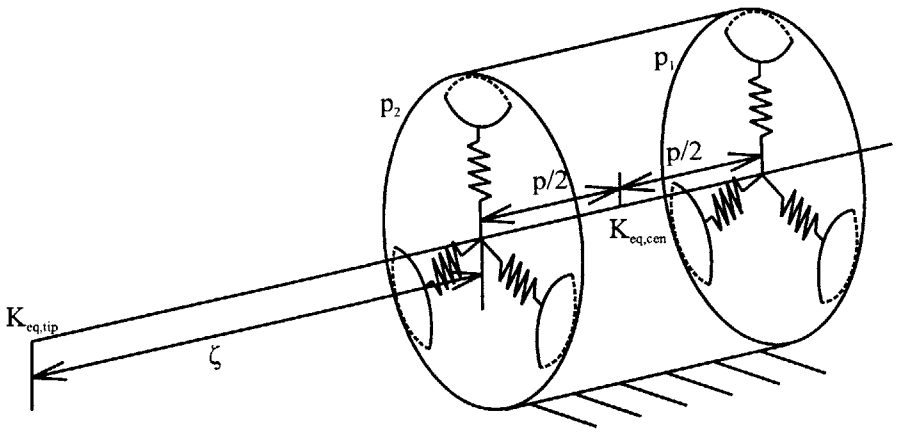

Figure 27: Equivalent stiffness at center and tip

To keep deflection of the end effector tip at a minimum, a minimum stiffness for the system is determined. Recall the transverse force shown in Figure 19; a maximum force of 1.6N is expected on the needle. To keep the deflection less than 5mm at the maximum transverse force, 1.6N, an equivalent stiffness of 0.32N/mm is required for $K_{eq,tip}$ of the clinical system. The equivalent stiffness of the laboratory prototype Beta is 10% of the clinical value to accommodate for lower actuator force than in a clinical device. The minimum stiffnesses in an individual plane and at the tip of the needle are shown in Table 2.

Table 2: Equivalent minimum stiffnesses in an individual plane of the device and at the tip of the needle

	$K_{eq,plane}$ (N/mm)	$K_{eq,tip}$ (N/mm)
Alpha Prototype	0.08	Not Applicable
Beta Prototype	0.25	0.03
Clinical Device	7.75	0.32

A system stiffness pattern is shown in Table 3. The spring rates in p_1 were chosen such that the even numbered modules have spring rates that are half of the odd numbered modules (see Figure 21). The odd numbered module spring rates of p_2 correspond to the even numbered module spring rates of p_1 and vice versa. The stiffness of spring 1 in p_1 was then increased to three times its current value and the stiffness of spring 4 in p_2 was reduced to half of its current value. These values produce an elliptical cone cylinder workspace appropriate for the prostate cancer application. These are also scalable based on the force requirements and the maximum force capabilities of the bistable actuator modules.

Table 3: Spring constants

	k_1 (N/mm)	k_2 (N/mm)	k_3 (N/mm)	k_4 (N/mm)	k_5 (N/mm)	k_6 (N/mm)
Plane 1	$3k$	$k/2$	k	$k/2$	k	$k/2$
Plane 2	$k/2$	k	$k/2$	$k/2$	$k/2$	k

The individual stiffnesses were modified to situate a larger portion of the workspace within the confines of the size of an average prostate. More specifically, the lower region of the prostate was most densely populated with end effector locations because this represents the peripheral zone, where most malignancies are found [62]. Workspace predictions will be presented and discussed in the next chapter.

3.4 Laboratory Prototype Beta Design Details

3.4.1 Simplifications

The Beta laboratory prototype is approximately 400mm in diameter, twice the allowable dimension for a clinical device (see Appendix A). The actuators themselves will need to be scaled to half their size to be appropriate for use in actual procedures.

The system stiffness is also only 10% of the necessary stiffness. These adjustments were made because the Beta prototype is designed for manufacture by hand. Each actuator only contains two layers of polymer film, which results in much lower forces and stiffnesses than required in a clinical device.

3.4.2 Parallel Planes

Each plane produces a workspace of approximately an 16mm diameter circle. In order to produce the required workspace the two planes must be appropriately spaced. The distance between p_1 and p_2, p, must be half the distance from p_2 to the prostate, z_{drep}. Assuming the distance from the perineum to the prostate is approximately 100mm and giving the planes adequate space to accommodate the size of the actuators, p should be 200mm and z_{drep} should be 400mm. Then, p_2 of the device should be placed 300mm from the perineum as shown in Figure 28. As shown in Section 4.2, these dimensions produce a desirable workspace and keep forces and moments on the manipulator at reasonable levels for a laboratory prototype.

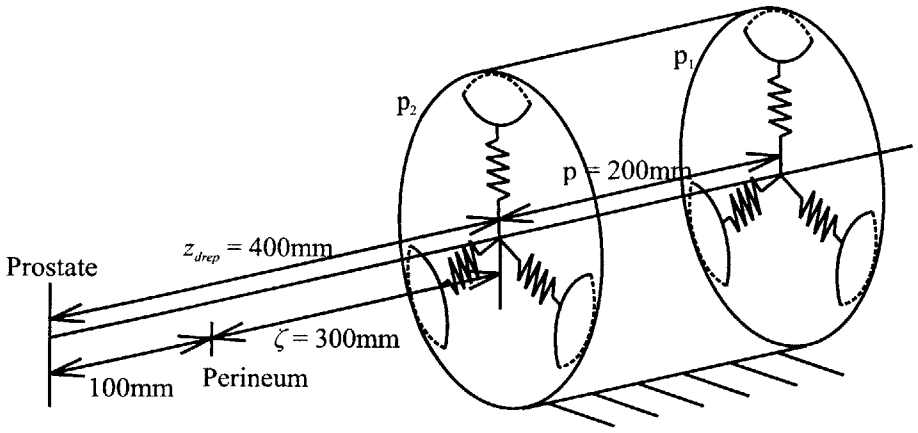

Figure 28: Spacing of planes and device

All bistable actuators are inserted between two side plates as shown in Figure 29. The bistable actuators are localized by slots cut in each side plate. The side plates are held together by spacers to achieve a precise distance between the plates (see Section A.4).

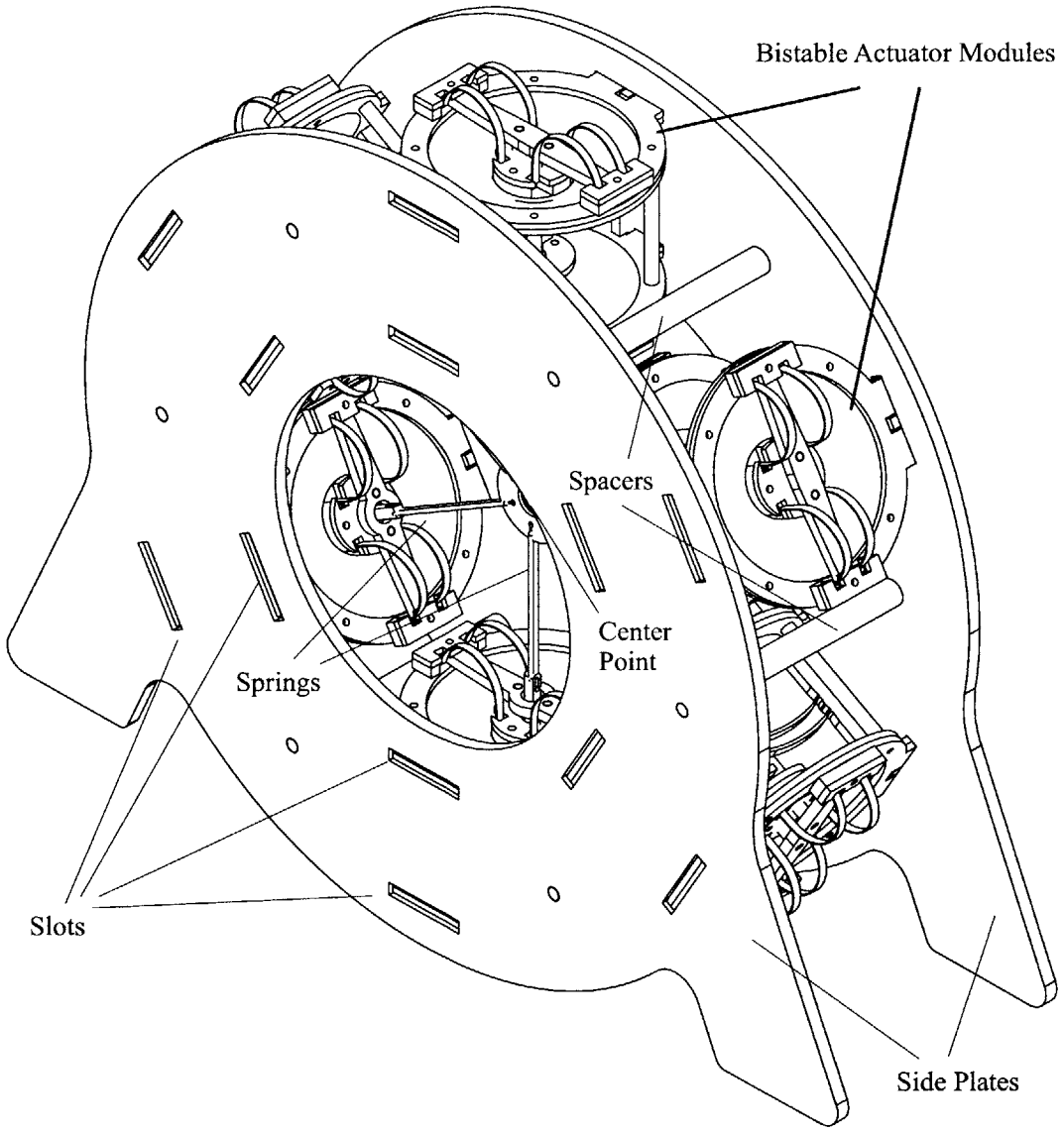

Figure 29: Plane of device

The legs of the device are higher than the bottom of the plane so that it can sit on a cradle inside an MRI as shown in Figure 30. It is clear that there is no room for a patient's legs in this design unless the device is placed very far from the patient. Recall that the device was made two times bigger for ease of manufacture.

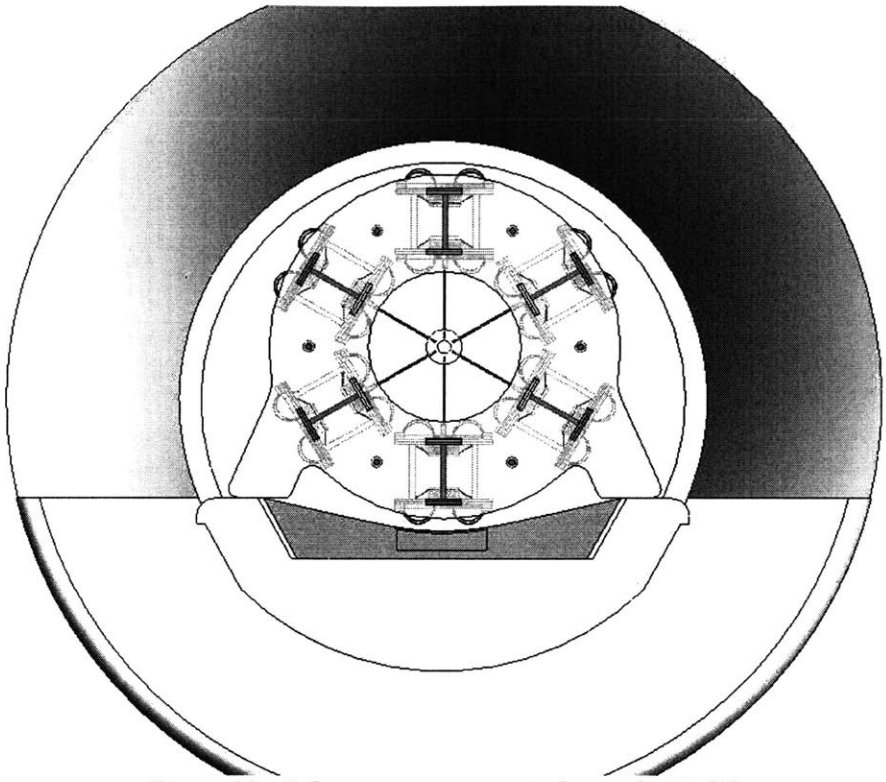

Figure 30: Laboratory prototype in bore of MRI [8]

3.4.3 Bistable Actuators

A solid model and a prototype of the bistable actuator are shown in Figure 31 and Figure 32 respectively. The bistable element is sandwiched between two DEAs. One end of the bistable element protrudes through the actuator nearest the center of the device and is connected to the rest of the device.

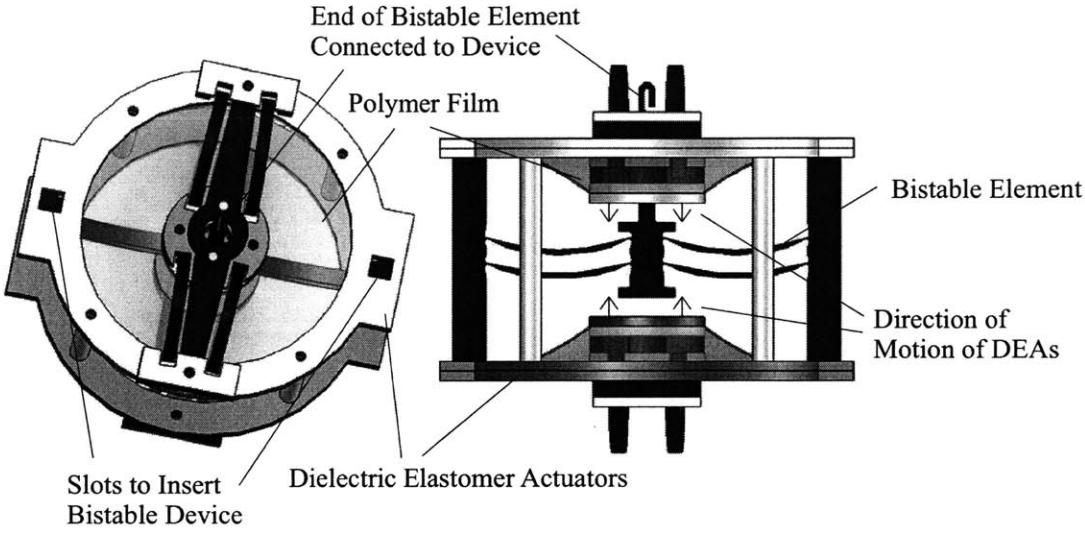

Figure 31: Bistable actuator

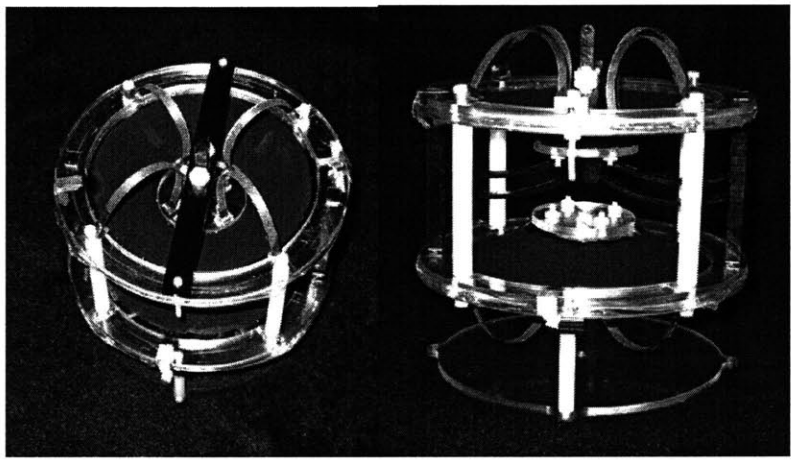

Figure 32: Bistable DEA prototype

The polymer film used in the actuators has an initial thickness of 1.5mm of 3M VHB 4905/4910. The film must be prestretched in order to avoid buckling. The actuators are designed with a film prestretch of λ^2=14 resulting in a final film thickness of 0.1mm [46]. Two layers of film are used in each actuator, so the total unactuated film thickness is 0.2mm. By applying 8.5 to 10kV, the actuators produce 2.5 to 3N of usable force and are capable of extensions of 14mm.

The bistable element (Figure 33) is designed such that these actuators could effectively flip the element and produce precise strokes. This part is cut from 5.2mm thick Delrin using a CNC machine to ensure accurate dimensions (see Section A.2). The 1.5mm thick leaf springs are left attached by thin, ~0.3mm flexures on either side. In order to make the device bistable, the outer edges are compressed causing the center piece to shift up or down to a stable position (see Figure 11) [49].

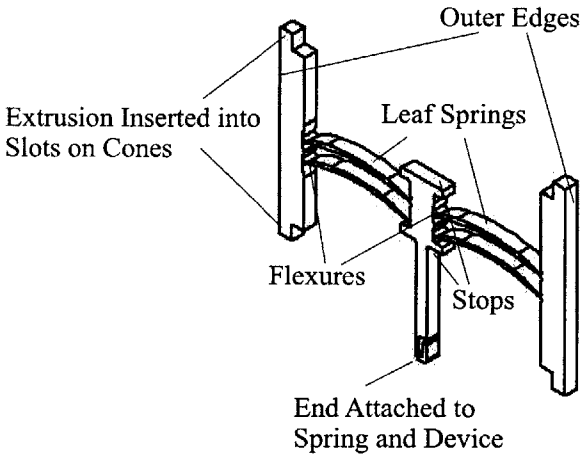

Figure 33: Design of bistable element for laboratory prototype

The bistable device is inserted into slots in the actuators (Figure 31), which provides a loose constraint for the preload of the bistable device. These slots are cut with a laser cutter, which does not provide high enough accuracy to ensure identical preloads. Instead, the side plates shown in Figure 29 are used to apply the correct and the same preload to all bistable elements yielding identical force profiles on each bistable element.

By constraining the outer edges of the bistable elements 2mm less than the dimension they are cut, the force profile shown in Figure 34 is achieved. The device extends slightly beyond 12mm so that the 14mm stroke of the actuators is sufficient to flip the bistable element. A stop is placed on either side of the bistable device to ensure the stroke of the bistable element is exactly

12mm. Other forces imposed on the device by the other bistable actuator modules and excessive external forces could affect the total deflection if the device were not attached in this manner.

The difference in force seen in Figure 34 of approximately 0.2N on the return stroke is due to hysteresis loses in Delrin.

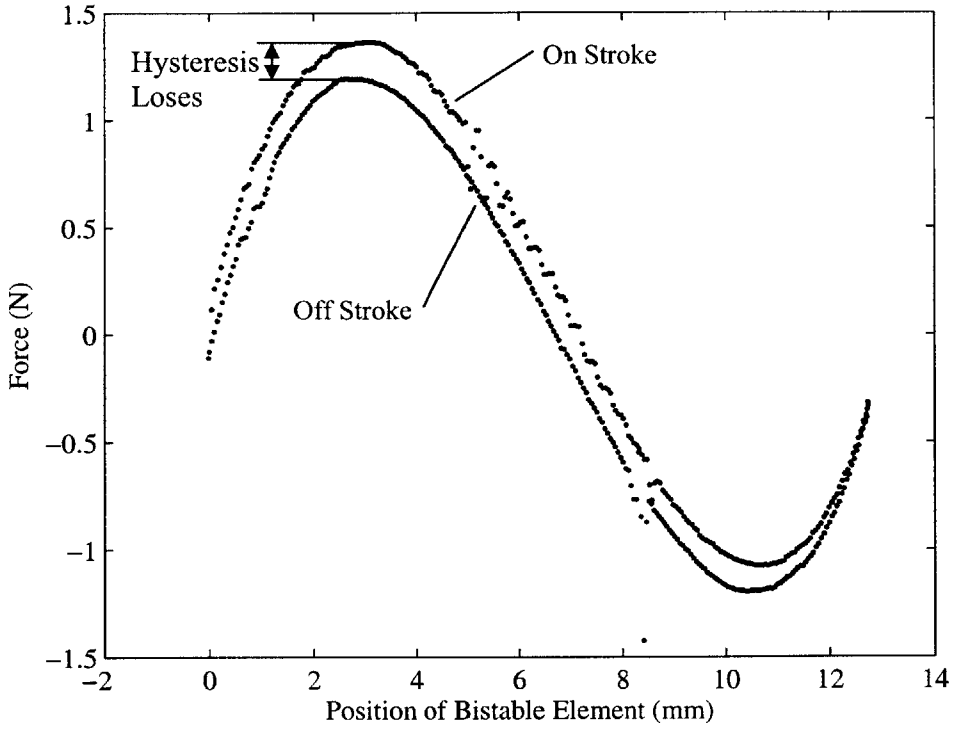

Figure 34: Force profile of bistable element

Because the bistable device is acting against the actuator for part of the stroke, the total output force of the bistable actuator module is approximately half the total output force of the actuator [46].

3.4.4 Maximum System Stiffness

The maximum stiffness of laboratory prototype Beta is limited by the force output of the actuators. The stiffness is approximately one tenth the required stiffness value, as noted in Section 3.3.

The actuators are capable of producing 3N. When coupled with a bistable element, the output force is approximately 1.5N. The maximum deformation of the stiffest spring, k_1 in p_1, is 4.6mm. Therefore, the maximum stiffness of each actuator module must be less than 1.5N/4.6mm and is set at 0.3N/mm. Recalling Table 3, k is set to 0.1N/mm to ensure that the bistable device only flips when actuated and does not flip due to internal forces. The stiffness values of the laboratory prototype due to this constraint are shown in Table 4. These values result in a minimum equivalent stiffness of 0.03N/mm using Equation (3.11).

Table 4: Laboratory prototype stiffnesses

	k_1 (N/mm)	k_2 (N/mm)	k_3 (N/mm)	k_4 (N/mm)	k_5 (N/mm)	k_6 (N/mm)
Plane 1	0.3	0.05	0.1	0.05	0.1	0.05
Plane 2	0.05	0.1	0.05	0.05	0.05	0.1

3.5 Laboratory Prototype Alpha

The Alpha laboratory prototype is a simplified version of the Beta prototype. Prototype Alpha has three bistable actuators in one plane as shown in Figure 35. All spring rates are equal and approximately 0.05N/mm, which results in an equivalent minimum stiffness at the center of the plane, $K_{eq,cen}$, of 0.09N/mm. These additional simplifications on the Beta prototype were made such that the Alpha prototype could be built by hand in a limited time frame.

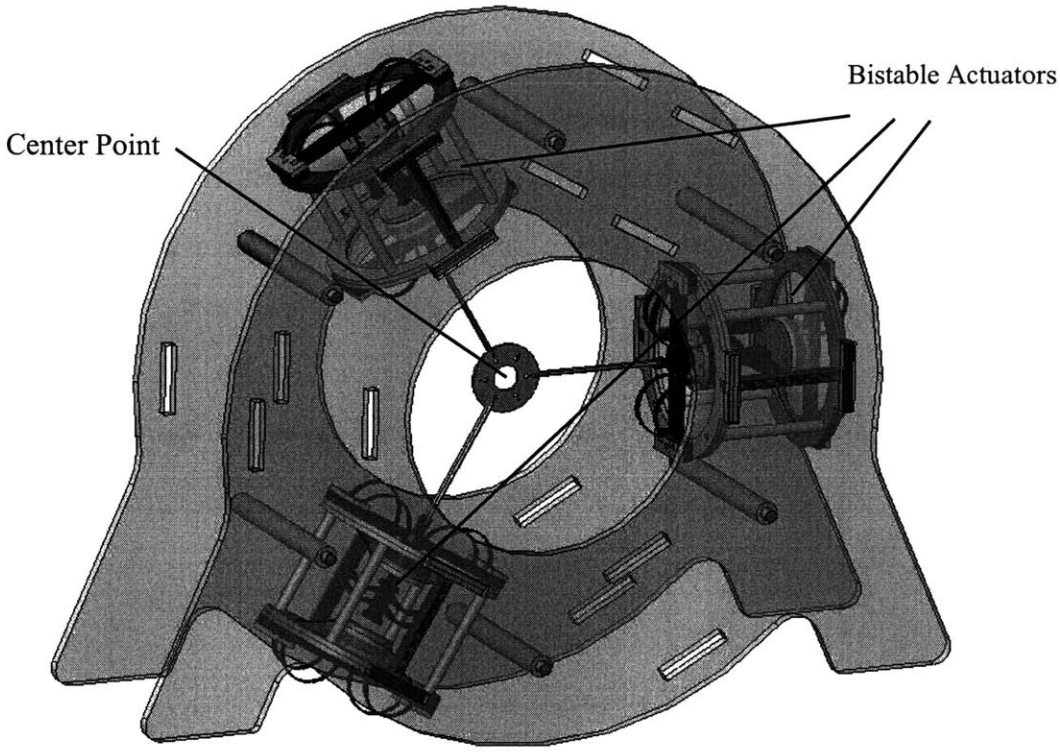

Figure 35: Solid model of laboratory prototype Alpha

3.6 Clinical Device Design

3.6.1 Size and Workspace Considerations

In order for this design to be feasible for clinical applications, the device must be scaled to half the laboratory prototype size. However, the workspace must remain the same. There are several ways to achieve this goal. The most logical is to reduce the size of the actuators themselves. This would bring the outer dimension of the device to 200mm in diameter. However, the horizontal separation of the planes and the distance to the perineum would need to be considered because the displacement of the actuators and bistable elements would also be cut in half.

If the actuators are reduced to half their size and their displacements are half their current displacements, the workspace will be reduced to 8mm in diameter at each plane. This requires that p be set at 100mm, z_{drep} at 400mm and ζ at 300mm (see Table 5). This produces the same size workspace as the laboratory prototype Beta design.

Table 5: Plane spacing of prototype Beta and clinical device

	p (mm)	z_{drep} (mm)	ζ (mm)
Prototype Beta	200	400	300
Clinical Device	100	400	300

3.6.2 Minimum System Stiffness

Using the values in Table 3, Equation (3.7) becomes:

$$\begin{bmatrix} f_x \\ f_y \end{bmatrix} = \begin{bmatrix} 1.5\sqrt{3}k & 0 \\ 0 & 5k \end{bmatrix} \begin{bmatrix} dx \\ dy \end{bmatrix} \tag{3.12}$$

for p_1 and the following for p_2:

$$\begin{bmatrix} f_x \\ f_y \end{bmatrix} = \begin{bmatrix} 1.5\sqrt{3}k & 0 \\ 0 & 2.5k \end{bmatrix} \begin{bmatrix} dx \\ dy \end{bmatrix} \tag{3.13}$$

As discussed in Section 3.3, the stiffness at the tip of the needle is dependent on the spacing of the planes. The spacing determined in Section 3.6.1, where p is 100 and ζ is 300, is used. Minimum equivalent stiffness at each plane occurs when θ is 0 and $\pi/2$. Solving Equation (3.11) using 0.32N/mm as a minimum stiffness for the entire system, the minimum value of k is 3.1N/mm. The required stiffness of each spring for the clinical system is given in Table 6.

Table 6: Numerical theoretical stiffness constants

	k_1 (N/mm)	k_2 (N/mm)	k_3 (N/mm)	k_4 (N/mm)	k_5 (N/mm)	k_6 (N/mm)
Plane 1	9.3	1.5	3.1	1.5	3.1	1.5
Plane 2	1.5	3.1	1.5	1.5	1.5	3.1

3.7 Other Applications of System Design

It is possible to adjust these values in order to achieve different workspace volumes and overall stiffness that would accommodate other applications. By changing the value of spring 1 in plane 1 from $3k$ to k and the value of spring 4 in plane 2 from $k/2$ to k, the workspace becomes a circular cone cylinder rather than an elliptical cone cylinder. The requirements of the system can dictate the spring relationships in order to change the shape of the workspace. The spring rates can also be scaled up or down to increase or decrease overall stiffness as shown in Section 3.4.4 and Section 3.6.2. By moving the planes closer together and further away from the target, the workspace accuracy will be decreased, but the area covered will be increased. Likewise, the opposite will increase the accuracy by reducing the size of the workspace.

3.8 Summary

This chapter described the use of DEAs in an MRI compatible needle manipulator. The DEAs are used in a bistable manner as dictated by an intensive failure study. To achieve high precision, the bistable DEAs are modulated by added compliance to achieve an elastically averaged plane of actuators. Parallel planes are used to produce the required workspace. Size, workspace and force requirements are considered in the design and are analyzed in Chapter 4.

CHAPTER

4

ANALYSIS AND RESULTS

4.1 Introduction

MATLAB® mathematical models are used to validate the system design. Appropriate design parameters are determined to achieve the required workspace and evaluated. A model using solenoids instead of DEAs is constructed to demonstrate the system concept and to validate the Matlab calculations. Finally, laboratory prototype Alpha is constructed with DEAs and tested inside the bore of an MRI to demonstrate concept feasibility.

4.2 Workspace Analysis of Beta Prototype

The design parameters in Chapter 3 were developed for the prostate cancer detection and treatment needle manipulator. The workspace of the device, shown at a needle penetration of 110mm in Figure 36 and at any penetration from 60 to 130mm in Figure 37, meets the workspace requirements. The depth of 110mm was chosen for an average distance from the perineum of 70mm and an average size prostate of 40mm as discussed in Section 2.3.2. Assuming these values, 110mm would be the maximum extent the needle would need to traverse. The device has a workspace of an elliptic cone cylinder. This workspace is much larger than a normal prostate. However, prostate are often enlarged when biopsy and treatment procedures are required, and the workspace is meant to accommodate for this. Slices of the workspace at different depths are shown in Figure 38.

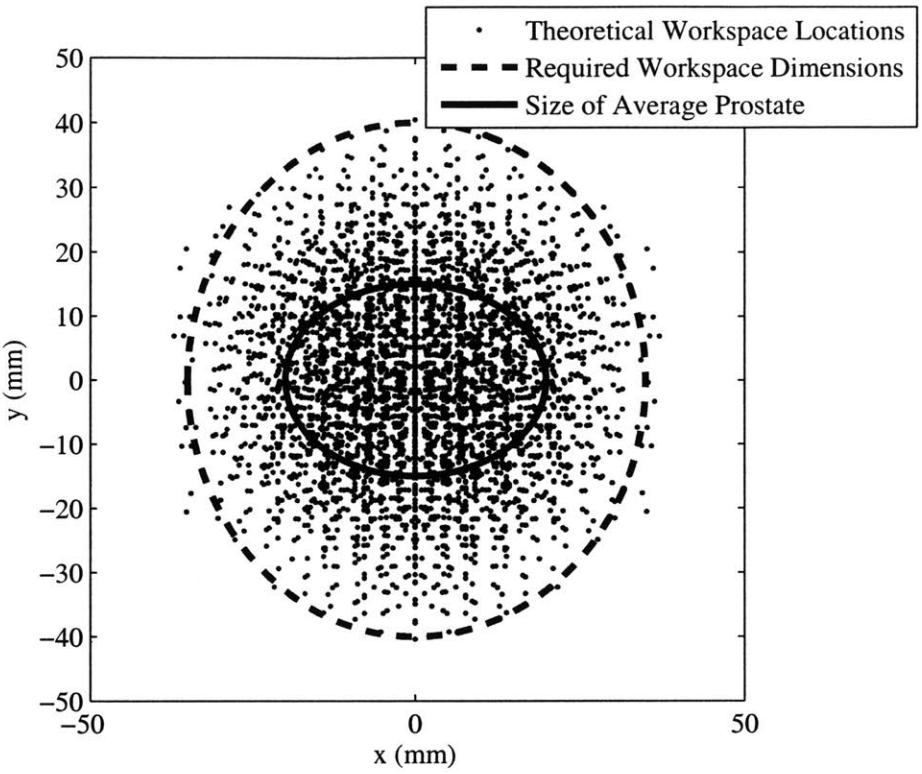

Figure 36: Theoretical workspace at 110mm beyond perineum wall

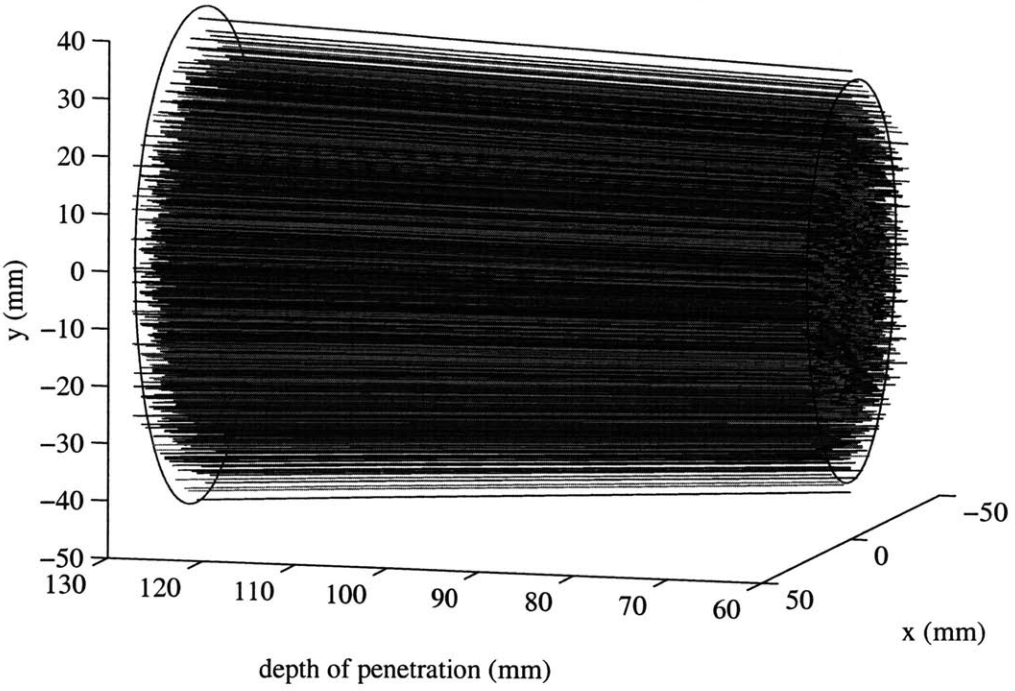

Figure 37: Workspace of MRI compatible needle manipulator at the prostate

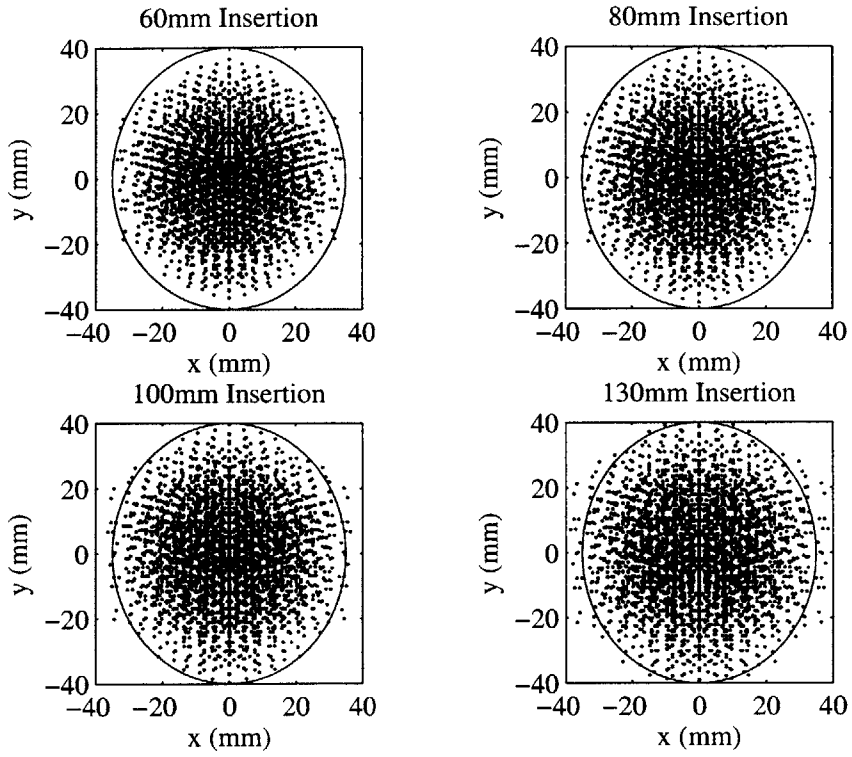

Figure 38: Workspace at different insertion depths

Using the required workspace and potential end effector locations, Equation (3.6) gives an approximate accuracy of ±0.52mm. The accuracy using a typical rectangular template of 70mm by 80mm with holes 5mm apart is ±2.5mm. The average accuracy of the Beta prototype using actual end effector locations and the standard deviation at different distances from the perineum are shown in Table 7.

Table 7: Average accuracy and standard deviation of Beta prototype

Distance from Perineum	60mm (mm)	110mm (mm)	130mm (mm)
Average Accuracy	0.18	0.21	0.22
Standard Deviation	0.18	0.20	0.21
Maximum Accuracy	1.38	1.57	1.65

More importantly, the target in the prostate can be any random point in the required workspace. The minimum distance from the closest possible end effector point to a random point in the required workspace was calculated using the typical template and the DEA manipulator design as shown in Figure 39 and Figure 40.

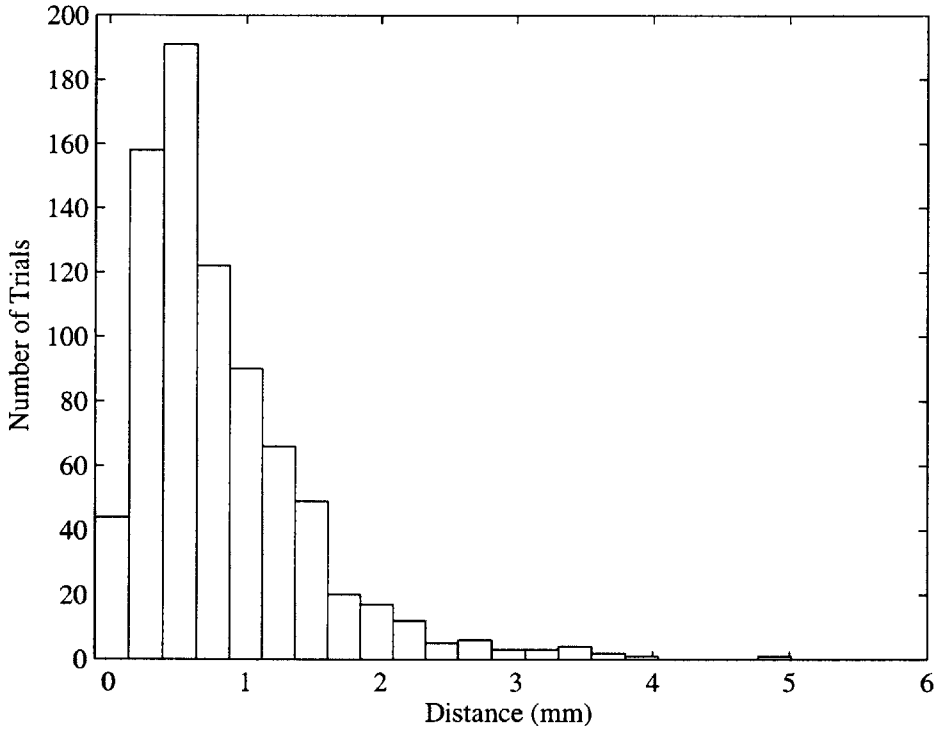

Figure 39: Minimum distance from end effector of Beta prototype to possible target location in required workspace

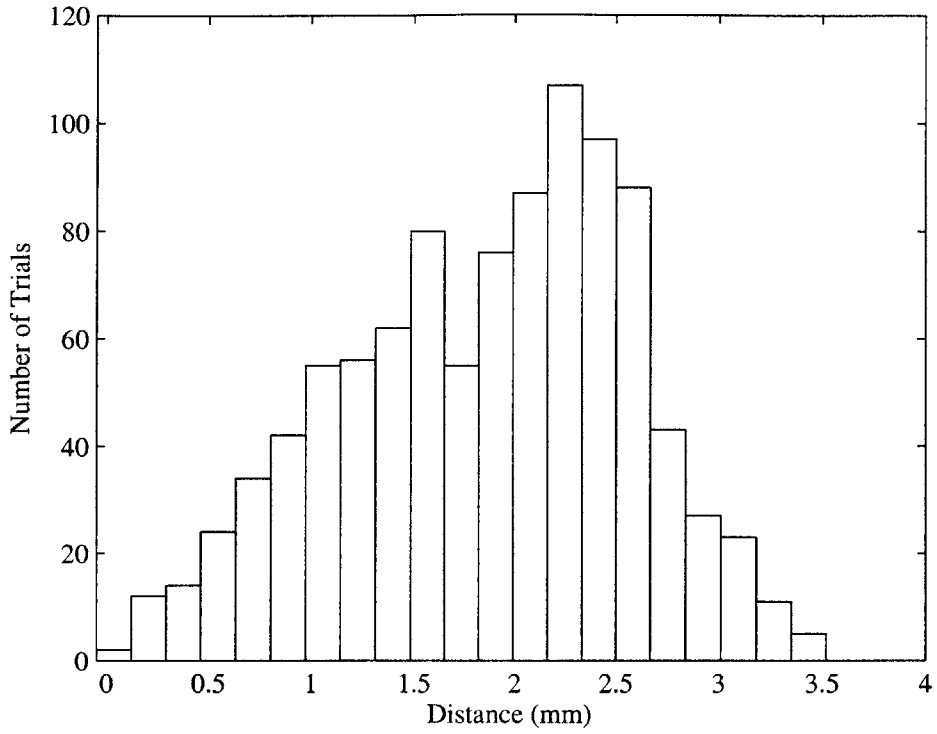

Figure 40: Minimum distance from needle tip using BWH template to possible target location in required workspace

The calculations were performed using the size of an average prostate. It was assumed that the prostate could extend anywhere from 60 to 130mm beyond the perineum. The prostate was represented, for these calculations by an elliptic cylinder, with a major diameter of 40 mm and a minor diameter of 20mm, 70mm deep as shown in Figure 14 and Figure 36 [16]. The results are shown in Figure 41. This calculation was not done for the template because the holes are evenly spaced and would result in statistically equivalent values as those shown in Figure 40. The average distance, δ, standard deviation, σ, and maximum distance, Max, are shown in Table 8.

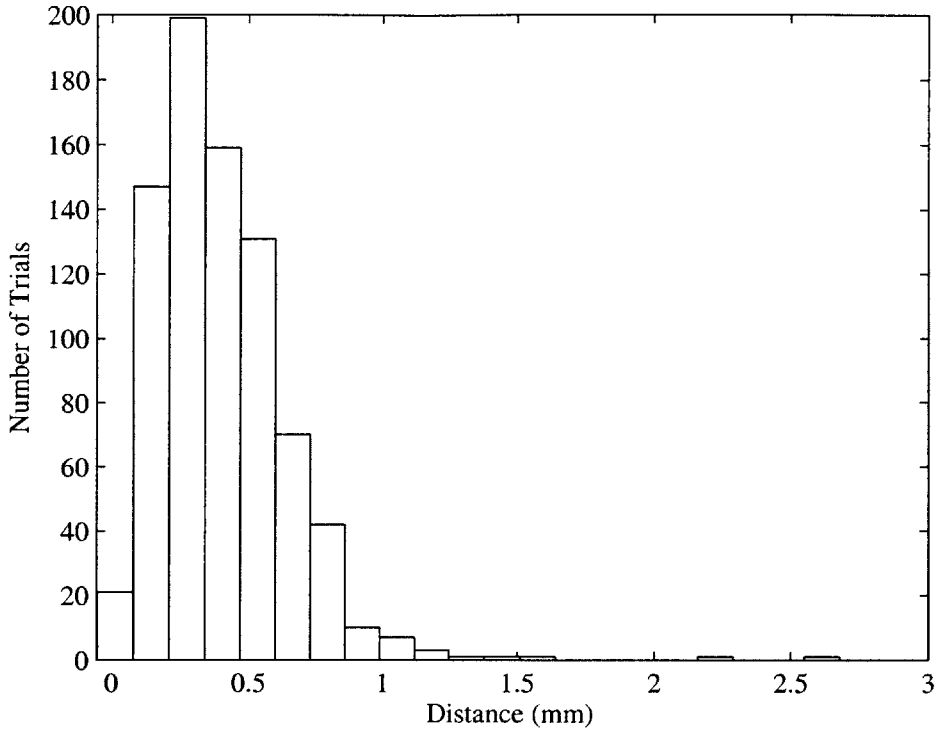

Figure 41: Minimum distance from end effector of Beta prototype to possible target location in average prostate

Table 8: Statistics for distance from a random point in the workspace and prostate workspace to the nearest possible end effector location

	δ (mm)	σ (mm)	Max (mm)
Typical Template	1.9	0.7	3.3
Beta Prototype – required workspace	0.82	0.68	5.8
Beta Prototype – average prostate	0.39	0.23	1.8

It should be noted that these numbers represent the mechanical placement of the needle. They do not take into account the poor image quality associated with ultrasound or the inability to adjust for needle deflection and soft tissue deformation when using a template.

4.3 Stiffness Analysis of Beta Prototype

The stiffness of each plane of the laboratory prototype Beta and the equivalent stiffness are shown in Figure 42. The minimum stiffness of the Beta system is 0.03N/mm, 10% of the required clinical stiffness, which can be seen in Figure 43. These values result in a maximum possible force on any individual bistable actuator, specifically k_4 of p_2, of 1.5N without any external forces. This number is within the capabilities of two layer actuators.

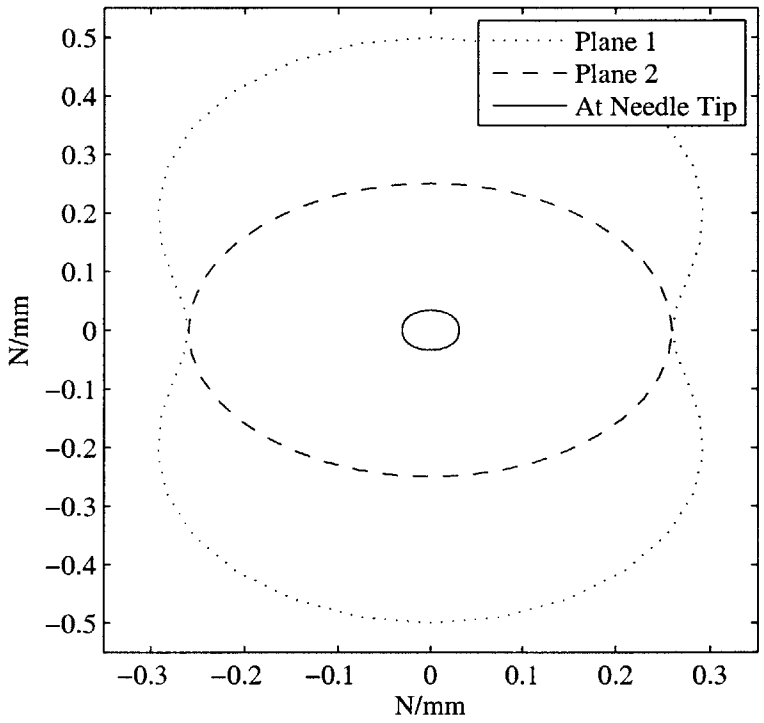

Figure 42: Theoretical stiffness of Beta prototype

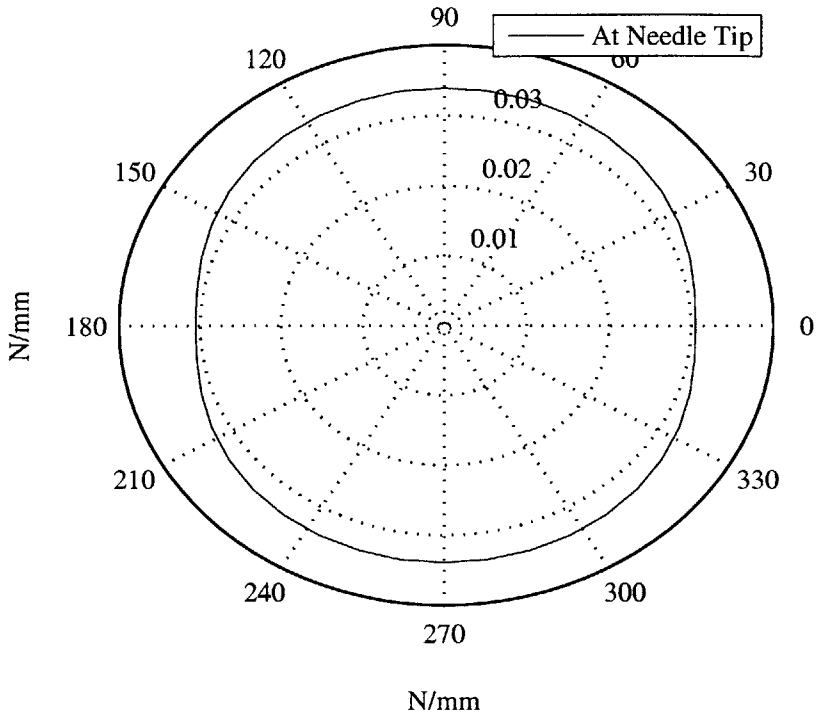

Figure 43: Theoretical stiffness at tip of Beta prototype

4.4 Workspace and Stiffness of Clinical Device

For a clinical device, the most force a bistable actuator would need to resist is 22N without any external forces. The possible addition of 1.6N would mean 23.6N on any one bistable actuator. The actuators would have to be able to produce slightly more than twice that force. Therefore, the actuators would need to be capable of producing 48N instead of the current 3. Theoretically, by increasing the number of layers from 2 to 32, the actuators should be capable of such forces. This would produce the stiffness ellipse shown in Figure 44.

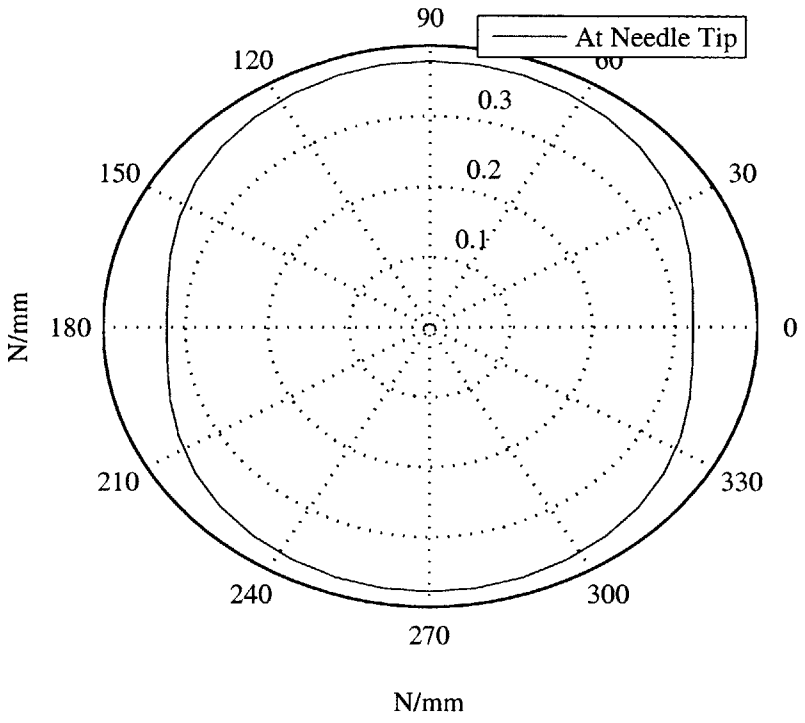

Figure 44: Theoretical stiffness at tip of clinical device

4.5 Experimental

Two experimental systems are designed and tested: a solenoid model for demonstration purposes and laboratory prototype Alpha.

4.5.1 Solenoid Demonstration

The system using solenoids instead of bistable actuators, shown in Figure 46, is used to demonstrate feasibility, repeatability and accuracy of the device. A laser pointer is set in place of a needle and the device is aligned parallel to the wall. The workspace of the system is determined by recording the location of the laser beam on the wall after actuation as shown in Figure 45 and Figure 46. Figure 49 shows the "end effector" locations of the solenoid device (the laser locations) and the expected locations from simulation.

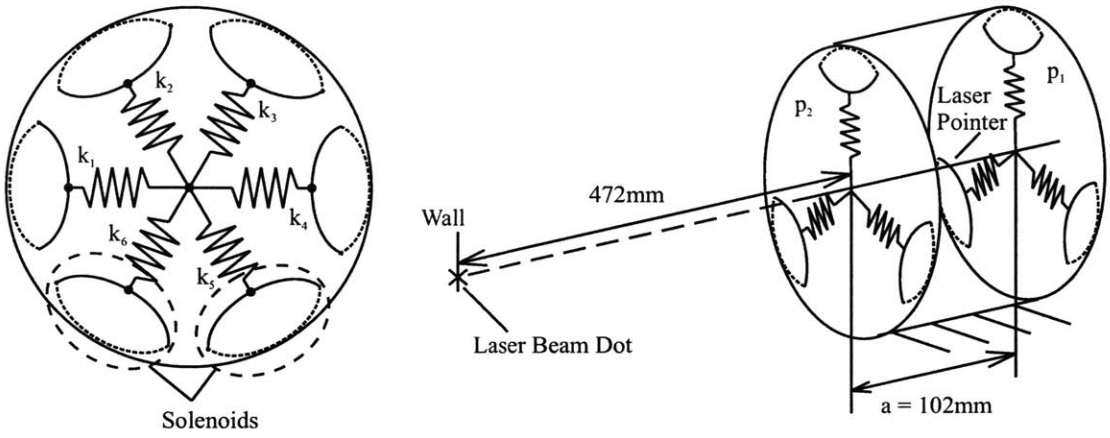

Figure 45: Diagram of solenoid demonstration

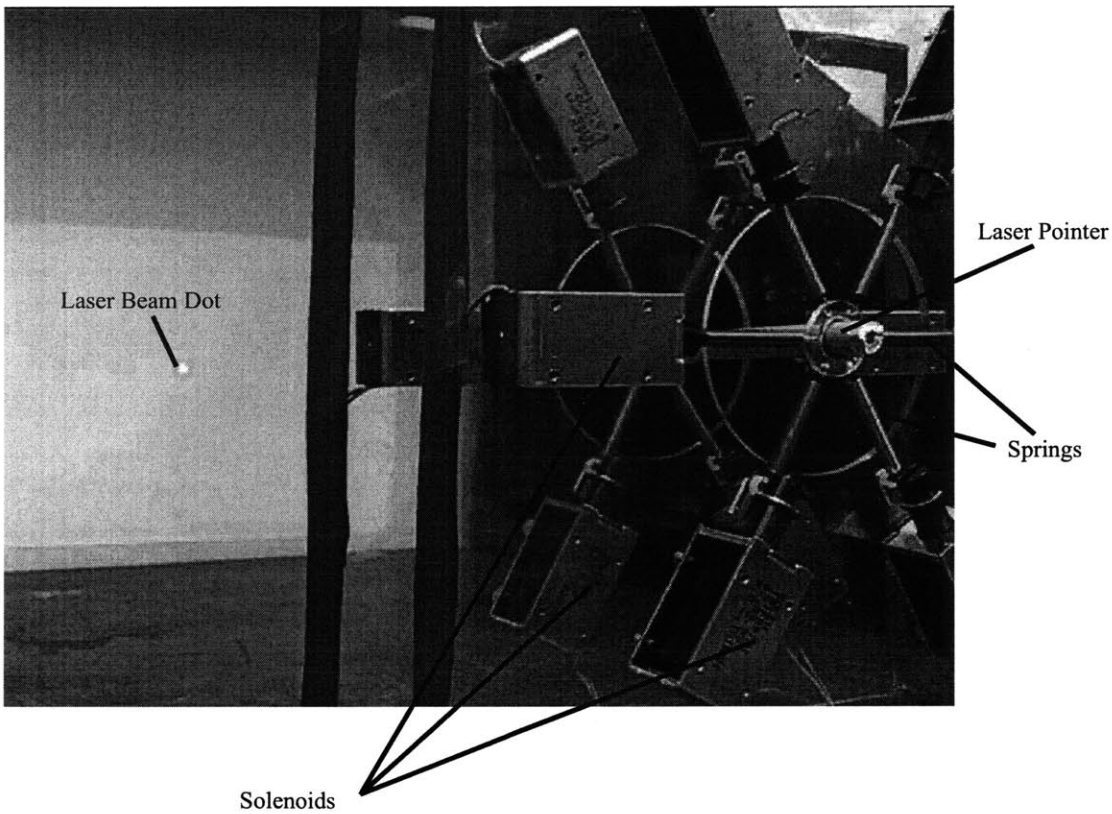

Figure 46: Solenoid demonstration

For simplicity, the solenoids are connected by springs with spring rates of 0.28N/mm and 0.03N/mm. On one plane, odd numbered solenoids are connected to springs with low spring constants, while on the other plane, even numbered solenoids are connected with springs with low

spring constants. The average experimental stiffness of each plane was 0.66 and that of the entire system at the middle of the two planes was 1.4. On average, the experimental values shown in Figure 47 are 91% and 93% of the expected stiffness values for each plane and the two planes together. This is likely due to using imprecise springs as well as the original assumption of very small motions and unaccounted system deflection. Larger deflections were used in order to measure the spring rates. The stiffness at the theoretical tip of the needle is shown in Figure 48.

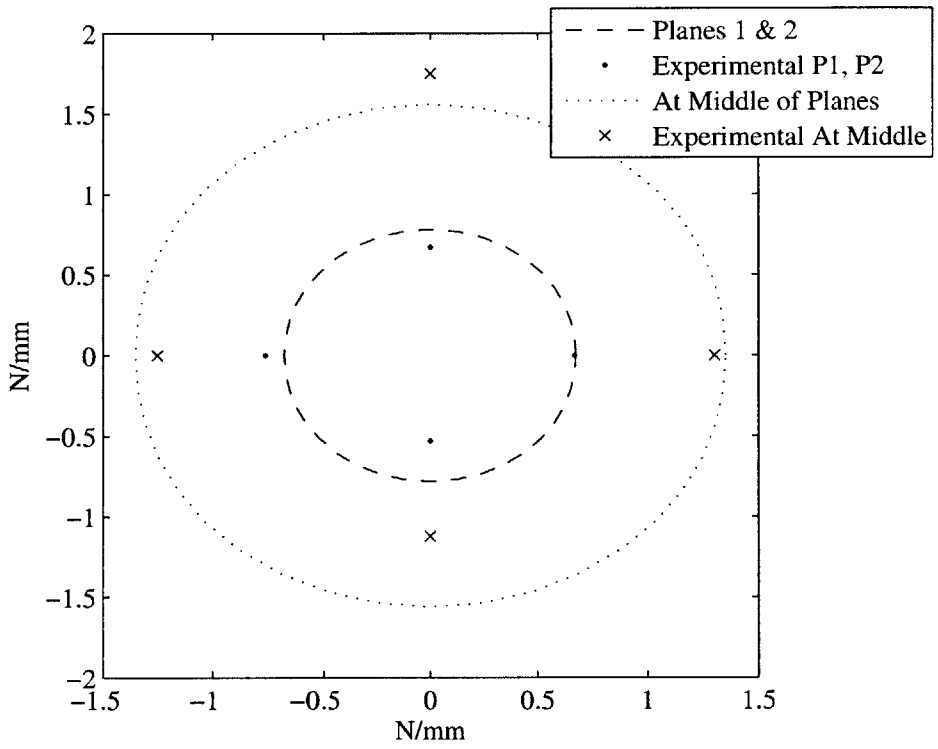

Figure 47: Theoretical and experimental stiffness of solenoid demonstration

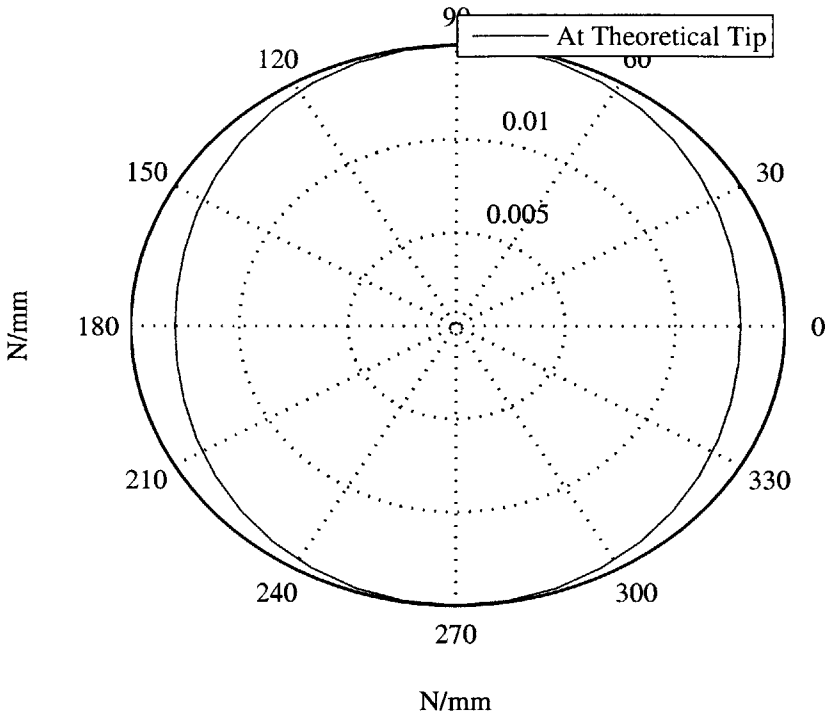

Figure 48: Theoretical stiffness at tip of solenoid demonstration

The planes are 102mm apart and the plane closer to the wall is 472mm from the wall. The initial length of the springs is 38mm and they were stretched to 61mm when all solenoids are on (pulling away from the center). Figure 49 shows the expected workspace points when calculated in Matlab and the actual points obtained using the solenoid setup. The average distance between the simulated and experimental points is 2.47mm.

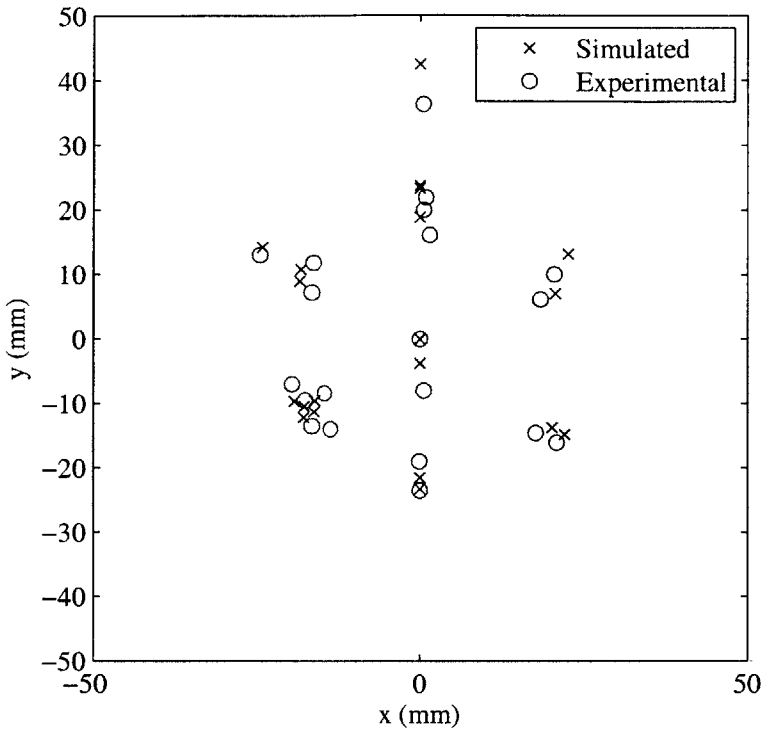

Figure 49: Workspace of solenoid laboratory demonstration

In a clinical device, better accuracy would be expected when moving a needle in free space by ensuring accurate spring constants.

4.5.2 Laboratory Prototype Alpha

Laboratory prototype Alpha is shown in Figure 50. Laboratory tests show that all actuators work and are capable of flipping the bistable elements.

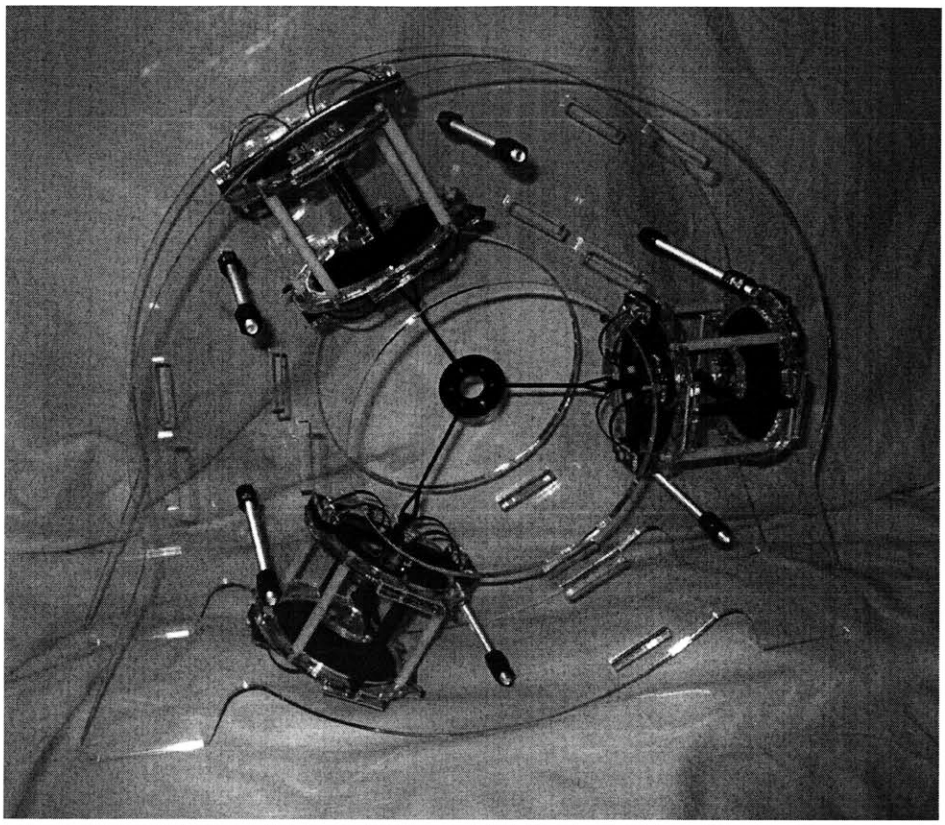

Figure 50: Laboratory prototype Alpha

Figure 51 and Figure 52 show the device and a phantom in the bore of the GE MRI at Brigham and Women's Hospital, inside which the laboratory prototype was designed to fit inside.

Figure 51: Laboratory prototype alpha in bore of MRI

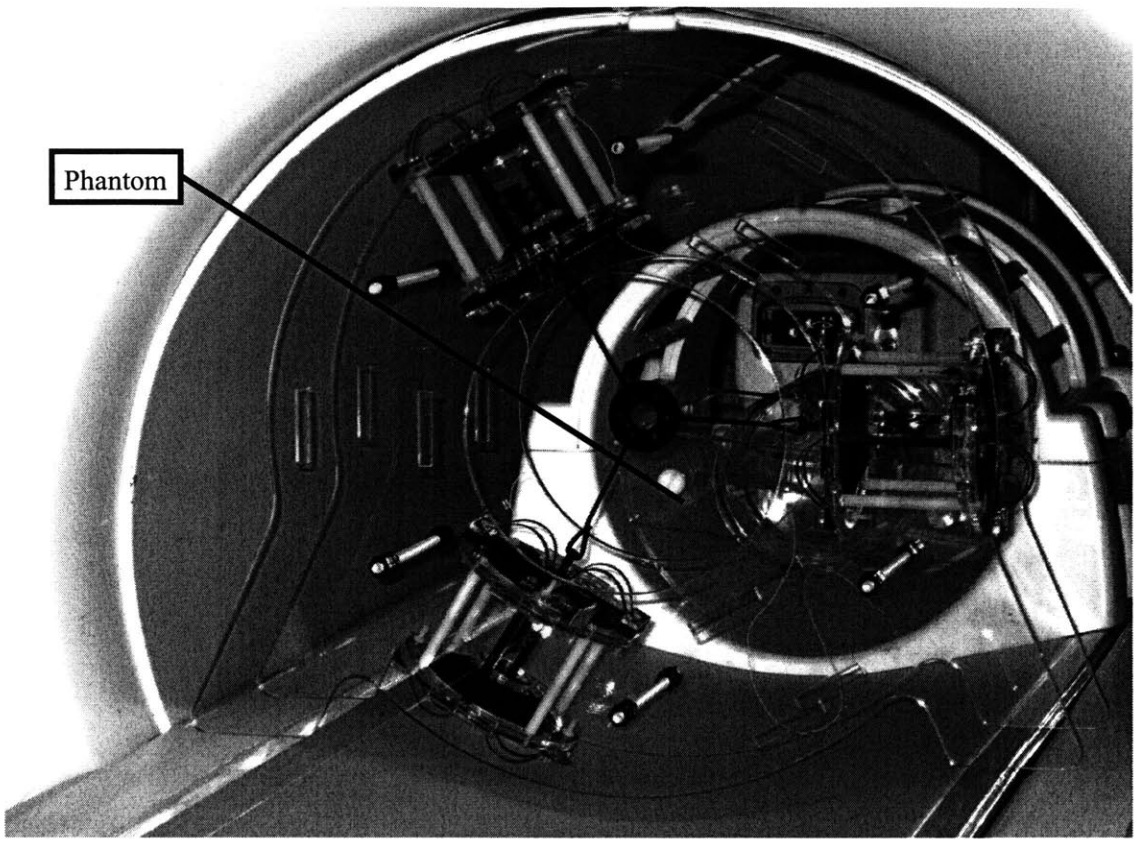

Figure 52: Laboratory prototype Alpha in bore of MRI with phantom

Images of a phantom with and without the prototype in the bore of the MRI show the compatibility of the device. Figure 53 shows the results of an experiment performed to determine if the device was putting out electromagnetic interference using a bistable actuator module. An image taken without the actuator (top left) is used to establish a 'baseline' for comparison. After placing the actuators inside the bore, another image is taken with the actuators off (top right) and shows no noise. When the actuators are turned on, the image (bottom left) shows noise in the form of two broad horizontal lines. When the RF pulse (which perturbs the magnetic field) is turned on, the image of the phantom is created (bottom right) and the noise is not detected [23].

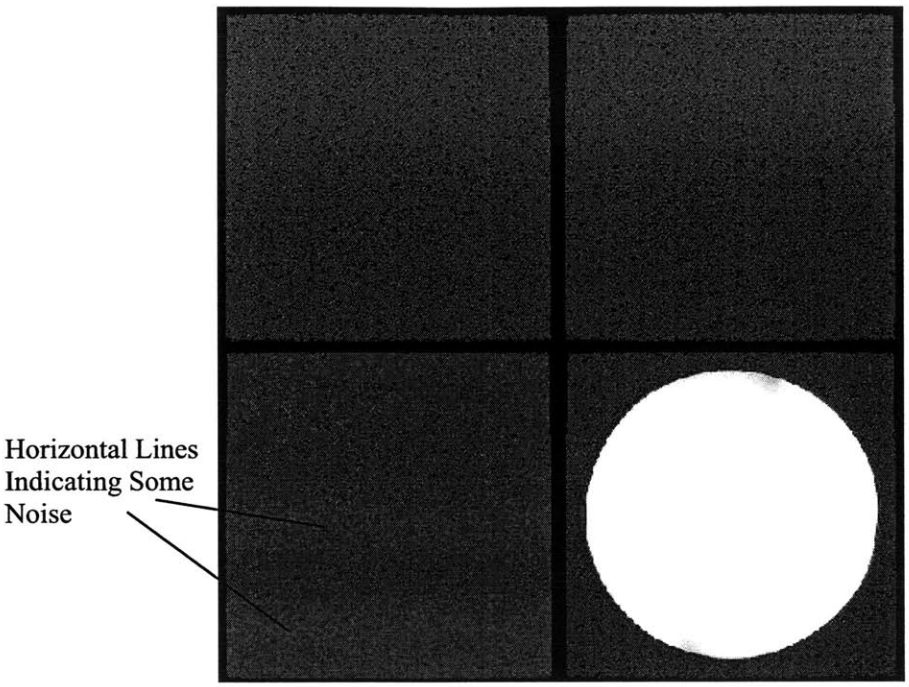

Figure 53: Noise testing: without actuator (top left), with actuators off (top right), with actuators on (bottom left), with actuators on and MRI RF excitation pulse on (bottom right)

Figure 54 and Figure 55 show images from susceptibility tests. These tests are concerned with possible distortion of the edges of the phantom. Figure 54 shows a front view of the phantom. The dark line in the center of the images is a piece of plastic (a part of the phantom) and the dark spot on the top of the images is an air bubble. Again, images are taken without any actuators to establish a baseline. Then, a single actuator is placed directly on top of the phantom. Figure 54 shows the results of imaging without the actuator (left), with the actuator on top of the phantom (middle) and with the actuator on top of the phantom and turned on (right). No distortion is seen on the edges of the phantom [23].

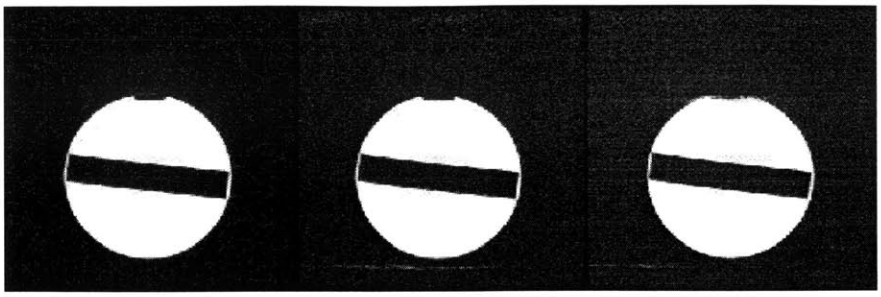

Figure 54: Susceptibility testing: without actuator (left), with actuator off (middle), with actuator on (right)

Figure 55 shows the results of tests with prototype Alpha. These images show a top view of the phantom used in the previous test. A baseline image (top left) shows the geometry of the phantom. A worse-case scenario is tested with Alpha touching the phantom with all actuators turned on (top right). A more realistic situation is tested with Alpha in its working location, further from the center of the magnet. Images are shown with the actuators off (bottom left) and with all the actuators turned (bottom right).

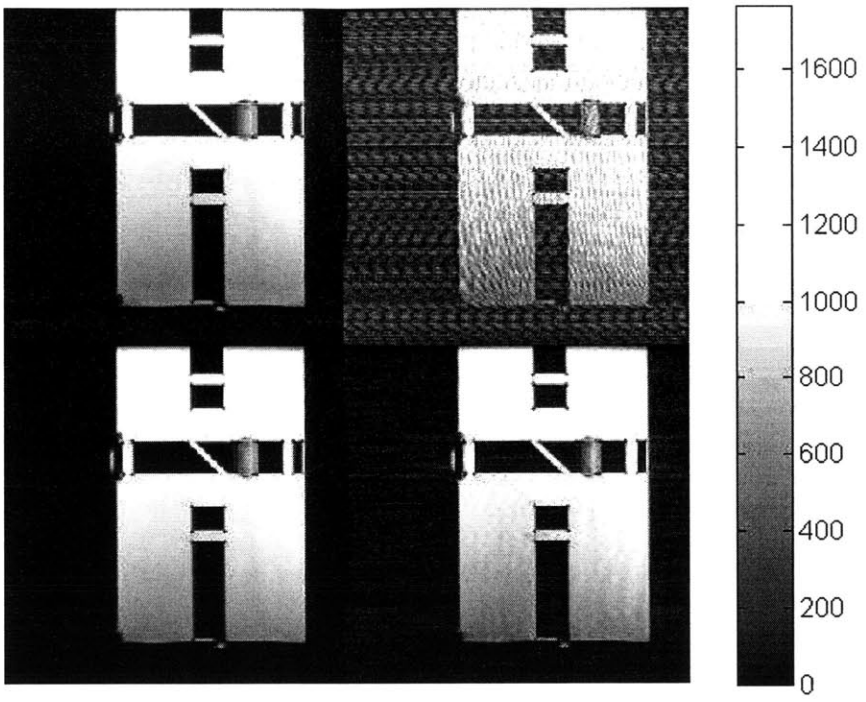

Figure 55: Susceptibility testing: without actuator (top left), with actuator on and touching phantom (top right), with actuator off in working location (bottom left), with actuator on in working location (bottom right)

According to Daniel Kacher and Dr. Joseph Roebuck of Brigham and Women's Hospital, even during worst case scenarios, there is no presence of susceptibility artifacts and electromagnetic interference is minimal when actuators are not powered. There is minor interference when the actuators are powered, but there has been no effort to filter interference effects.

The Alpha prototype contains small amounts of materials that may affect image quality. The aluminum parts (the spacers, see Figure 29) can generate eddy currents. Prototype Alpha uses a very small amount of nickel paint (approximately 10mg) for conductive leads, which is a ferromagnetic metal. The no power results show that these materials did not affect image quality. In any case, the aluminum parts and nickel paint can easily be substituted for better materials such as plastic parts and silver (diamagnetic) paint or aluminum (paramagnetic) tape to reduce the risks of interference.

4.6 Summary

Provided multi-layer actuators can be fabricated, calculations and experiments show the needle manipulator developed in this research will meet the specifications set forth in Chapter 3 and established with researchers at Brigham and Women's Hospital. It also suggests that variations of this device can be applied for use in other MRI procedures that require high precision. MRI compatibility is confirmed through testing of the prototype inside the bore of an MRI with phantom images.

CHAPTER

5

CONCLUSIONS

5.1 Contributions of this Thesis

This thesis developed a design for an MRI compatible needle manipulator for prostate cancer detection and treatment. The key contribution of this work is the use of parallel planes and elastic averaging to achieve high precision in a binary robotic system. It also presents a biomedical application of DEAs.

Chapter 1 explains the motivation for this work. Prostate cancer affects many men and currently, there is no truly accurate way of diagnosing cancer exists. There has been in increase in research towards using MRI to help guide a needle to the prostate during biopsy and treatment. However, this requires the use of an MRI compatible robotic needle manipulator.

The size, force and workspace requirements of the device developed in conjunction with researchers at Brigham and Women's Hospital are established in Chapter 2. Laboratory prototype specifications and clinical device projections are presented.

The system design, stiffness and accuracy of the manipulator are developed in Chapter 3. The design of a laboratory prototype and a clinical device are detailed. Size and force requirements for a laboratory prototype are relaxed due to constraints of current manufacturing processes.

Chapter 4 presents simulated and experimental analysis and results. The stiffness of the laboratory prototype must be increased by increasing the number of layers of film in each actuator in the development of a clinical device. The actuators must also be scaled to half their

current size. Laboratory prototype Beta meets workspace requirements. Its workspace is comparable to the template used at BWH. The solenoid system demonstrates that the method of parallel planes of elastically averaged bistable actuators can effectively and repeatedly produce the workspace required at the prostate. Laboratory prototype Alpha is functional and shows MRI compatibility.

High precision in binary robotics using elastically averaged, parallel mechanisms is shown to be feasible. The concept of elastic averaging of bistable actuators is analyzed and shows promising results for the future of binary robotics. A potential application of polymer actuators is addressed.

5.2 Suggestions for Future Work

A design for the actual needle insertion is the next key step in the development of a robotic needle manipulator. The actuators and manipulator will need to be scaled to half their current size in order to fit between a patient's legs. Testing with phantoms and animal substitutes, such as fruit, is an important step towards clinical use that should take place both outside and within the bore of an MRI machine. Control of the device and coordination with the MR images will need to be addressed before clinical trials can occur.

This device, once fully developed can and should be adjusted to suit other applications. In particular, breast cancer treatment, which could be improved through in-bore MRI procedures, should be considered. Other applications could include elastography of the breast, prostate, liver and other organs to detect abnormalities.

REFERENCES

1 Alterovitz, R., Pouliot, J., Taschereau, r., Hsu, I-C.J., Goldburg, K., "Simulating Needle Insertion and Radioactive Seed Implantation," Medicine Meets Virtual Reality 11, J.D. Westwood et al. (Eds.), IOS Press, pp. 19-25, 2003.

2 Babaian, R.J., et al., "NCCN Clinical Practice Guidelines in Oncology: Prostate Cancer Early Detection, VI," 2006.

3 Berger, A.P., Gozzi, C., Steiner, H., Frauscher, F., Varkarakis, J., Rogatsch, H., Bartsch, G., Horninger, W., "Complications rate of transrectal ultrasound guided prostate biopsy: a comparison among 3 protocols with 6, 10 and 15 cores," Journal of Urology, Vol. 171(4), pp. 1478-80, 2004.

4 Brink, S., "Prostate cancer test's accuracy cited," *Los Angeles Times*, p. A16, 26 April 2007.

5 Chinzei, K., Kikinis, R., Jolesz, F., "MR Compatibility of Mechatronic Devices: Design Criteria," Medical Image Computing and Computer-Assisted Intervention, pp. 1020-1030, 1999.

6 Chinzei, K., Miller, K., "Towards MRI guided surgical manipulator," Med Sci Monit, Vol 7(1), pp. 153-163, 2001.

7 Claeyssen, R., Letty, R.L., Barillot, F., Lhermet, N., Fabbro, H., Guay, P., Yorck, M., Bouchilloux, P., "Mechanisms Based on Piezo Actuators," Smart Structures and Materials: Industrial and Commercial Applications of Smart Structures, SPIE, Vol. 4332, pp. 225-233, 2001.

8 DiMaio, S.P., Ph.D., Brigham and Women's Hospital, Private Communications, 2005-2007.

9 DiMaio, S.P., Fisher, G.S., Haker, S.J., Hata, N., Iordachita, I., Tempany, C.M., Kikinis, R., Fichtinger, G., "A Sytem for MRI-guided Prostate Interventions," International Conference on Biomedical Robotics and Biomechatronics, Febuary 2006.

10 DiMaio, S.P., Salcudean, S.E., "Needle Steering and Model Based Trajectory Planning," Medical Image Computing and Computer-Assisted Intervention, 2003.

11 Elhawary, H., Zivanovic, A., Young, I., De Souza, N., Rea, M., McRobbie, D., Besant, C., Davies, B., Lampérth, M., "Development of a Master-Slave MRI Compatible Prostate Biopsy Manipulator," Medical Image Computing and Computer-Assisted Intervention, 2006.

12 Emiliozzi, P., Corsetti, A., Tassi, B., Federico, G., Martini, M., Pansadoro, V., "Best approach for prostate cancer detection: a prospective study on tranperineal versus transrectal six-core prostate biopsy," Urology, Vol. 61(5), pp. 961-966, 2003.

13 Fichtinger, G., Kreiger, A., Susil, R., Tanacs, A., Whitcomb, L.L., Atalar, E., "Transrectal Prostate Biopsy Inside Closed MRI Scanner with Remote Actuation, under Real-Time Image Guidance," Medical Image Computing and Computer-Assisted Intervention, 2002.

14 Fisher, G.S., Iordachita, I., DiMaio, S.P., Fichtinger, G., "Design of a Robot for Transperineal Prostate Placement in MRI Scanner," IEEE International Conference on Mechanisms, 2006.

15 Fisher, H., Kutter, S., Vagner, J., Felden, A., Pfleiderer, S.O.R., Kaises, W.A., et al, "ROBITOM II, Robot for Biopsy and Therapy of the Mamma," IEEE international conference on systems, man & cybernetics, 2004.

16 Fu, L., Ng, W.S., Liu, H., O'Dell, W., Rubens, D., Strang, J., Schell, M.C., Brasacchio, R., Liao, L., Messing, E., Yu, Y., "Bouquet brachytherapy: Feasibility and optimization of conically spaced implants," American Brachytherapy Society, Vol. 4, pp. 59-63, 2005.

17 Gassert, R., Moser, R., Burdet, E., Bleuler, H., "MRI/fMRI-Compatible Robotic System With Force Feekback from Interaction With Human Motion," IEEE/ASME Transactions of Mechatronics, Vol. 11, pp. 216-224, 2006.

18 Grossfield, G.D., Carroll, P.R., "Prostate Cancer Early Detection: A Clinical Perspective," Epidemiologic Reviews, Vol. 23, pp. 173-180, 2001.

19 Hata, N., Jinzaki, M., Kacher, D., Cormack, R., Gering, D., Nabavi, A., Silverman, S.G., D'Amico, A.V., Kikinis, R., Jolesz, F., Tempany, C.M.C., MRI-guided prostate biopsy using surgical navigation software: device validation and preliminary experience."

20 Jamis-Dow, C.A., Choyke, P.L., Jennings, S.B., Linehan, W.M., Thakore, K.N., Walther, M.M., "Small (S3-cm) Renal Masses: Detection with CT versus US and Pathologic Correlation," Genitourinary Radiology, 198(3), pp.785-788, 1996.

21 Jemal, A., Murray, T., Ward, E., Samuels, A., Tiwari, R.C., Ghafoor, A., Feuer, E.J., Thun, M.J. Cancer Statistics, 2005. C.A.: A Cancer Journal for Clinicians, Vol. 55, pp. 10-30, 2005.

22 Jemal, A., et al, Cancer Facts and Figures 2007, American Cancer Society, 2007.

23 Kacher, D., Brigham and Women's Hospital, Private Communications, 2005-2007.

24 Kaplan, I., Oldenburg, N.E., Meskell, P., Blake, M., Church, P., Holupka, E.J., "Real time MRI-ultrasound image guided stereotactic prostate biopsy," Magnetic Resonance Imaging, Vol. 20, pp. 295–299, 2002.

25 Kataoka, H., Washio, T., Chinzei, K., Mizuhara, K., Simone, C., Okamura, A., "Measurement of the Tip and Friction Force Acting on a Needle During Penetration," Medical Image Computing and Computer-Assisted Intervention, 2002.

26 Kimura (Nishitai), A., Camp, J., Robb, R., Davis, B., "A Prostate Brachytherapy Training Rehearsal System – Simulation of Deformable Needle Insertion," Medical Image Computing and Computer-Assisted Intervention, 2002.

27 Kornbluh, R., Pelrine, R., Joseph, J., "Elastomeric Dielectric Artificial Muscle Actuators for Small Robots," in Proc. of the Materials Research Society Symposium, vol. 600, pp. 119-130, 1995.

28 Kornbluh, R., Pelrine, R., Pei, Q., Oh, S., Joseph, J., "Ultrahigh Strain Response of Field-Actuated Elastomeric Polymers," in Proc SPIE Smart Structures and Materials 2000 (Electroactive Polymer Actuators and Devices), vol. 3987, pp. 51-64, 2000.

29 Koseki, Y., Kikinis, R., Jolesz, F., Chinzei, K., "Precise Evaluation of Positioning Repeatability of MR-Compatible Manipulator Inside MRI," Medical Image Computing and Computer-Assisted Intervention, 2004.

30 Koseki, Y., Koyachi, N., Arai, T., Chinzei, K., "Remote Actuation Mechanism for MR-compatible Manipulator Using Leverage and Parallelogram," IEEE International Conference on Robotics and Automation, pp.652-657, 2003.

31 Kreiger, A., Susil, R.C., Ménard, C., Coleman, J.A., Fichtinger, G., Atalar, E., and L.L. Whitcomb, "Design of a Novel MRI Compatible Manipulator for Image Guided Prostate Interventions," IEEE Transactions on Biomedical Engineering, Vol. 52, No. 2, pp. 306-313, 2005.

32 Lagerburg, V., Moerland, M.A., Konings, M.K., van de Vosse, R.E., Lagendijk, J.J.W., Battermann, J.J., "Development of a tapping device: a new needle insertion method for prostate brachytherapy," Physics in Medicine and Science, Vol 51, pp 891-902, 2006.

33 Larson, B.T., Erdman, A.G., Tsekos, N.V., Yacoub, E., Tsekos, P.V., Koutlas, I.G., "Design of an MRI-Compatible Robotic Stereotactic Device for Minimally Invasive Interventions in the Breast," Journal of Biomechanical Engineering, Vol 126, Issue 4, pp. 458-465, August 2004.

34 Lichter, M., Sujan, V., Dubowsky, S., "Experimental Demonstrations of a New Design Paradigm in Space Robotics," in International Symposium on Experimental Robotics (ISER '00), Honolulu, HI, December 2000.

35 Lichter, M., Sujan, V., Dubowsky, S., "Computational Issues in the Planning and Kinematics of Binary Robots," in Proc. 2002 IEEE International Conference on Robotics and Automation, Washington D.C.

36 Margolis, S.M., The 2006 John Hopkins White Paper: Prostate Disorders, John Hopkins Medicine, 2006.

37 Masamune, K., Ji, L.H., Suzuki, M., Dohi, T., Iseki, H., Takakura, K., "A Newly Developed Stereotactic Robot with Detachable Drive for Neurosurgery," Medical Image Computing and Computer-Assisted Intervention, 1998.

38 Mukherjee, S., Murlidhar, S., "Massively Parallel Binary Manipulators," Transactions of the ASME, Vol 123, pp. 68-72, 2001.

39 Nag, S., Beyer, D., Friedland, J., Grimm, P., and R. Nath, "American Brachytherapy Society (ABS) Recommendations for Transperineal Permanent Brachytherapy of Prostate Cancer," International Journal of Radiation Oncology Biology Physics, Vol. 44, No. 4, pp. 789-799, 1999.

40 Nag, S., Ciezki, J.P., Cormack, R., Doggett, S., DeWyngaert, K., Edmundson, G.K., Stock, R.G., Stone, N.N., Yu, Y., Zelefsky, M.J., "Intraoperative planning and evaluation of Permanent Prostate Brachytherapy: Report on the American Brachytherapy Society," International Journal of Radiation Oncology Biology Physics, Vol. 51, No. 5, pp. 1422-1430, 2001.

41 Naganou, H., Iseki, H., Masmune, K., "MRI Compatible Modular Designed Robot for Interventional Navigation – Prototype Development and Evaluation –," Medical Image Computing and Computer-Assisted Intervention, 2004.

42 Oikawa, M., Yamasaki, M., Takeda, H., Itagaki, H., Tajima, F., Sudo, K., Hirose, M., "Intra-operative guidance with real-time information of open MRI and manipulators using coordinate-integration module," SPIE, Volume 5029, pp. 653-660 , 2003.

43 Okazawa, S., Ebrahimi, R., Chuang, J., Salcudean, S.E., Rohling, R., "Hand-Held Steerable Needle Device," IEEE/ASME Transactions on Mechatronics, Vol. 10, No. 3, pp. 285-296, 2005.

44 Pieper, D.L., "The Kinematics of Manipulators under Computer Control," Ph.D. dissertation, Stanford Univ., Palo Alto, CA, 1968.

45 Pinkstaff, D.M., Igel, T.C., Petrou, S.P., Broderick, G.A., Wehle, M.J., Young, P.R., "Systemic transperineal ultrasound guided template biopsy of the prostate: Three-year experience," *Urology*, Vol. 65, pp. 735-739, 2005.

46 Plante, J.S., "Dielectric Elastomer Actuators for Binary Robotics and Mechatronics, PhD Thesis, Department of Mechanical Engineering, MIT"

47 Plante, J.S., DeVita, L., and Dubowsky, S. "A Road to Practical Dielectric Elastomer Actuators Based Robotics and Mechatronics: Discrete Actuation." Proceedings of the 2007 Conferences on Smart Structures, San Diego, California, (Invited Plenary), March 2007.

48 Plante, J.S., Dubowsky, S., "Large-scale failure modes of dielectric elastomer actuators", International Journal of Solids and Structures, Vol. 43, pp. 7727-7751, 2006.

49 Plante, JS., Santer, M., Dubowsky, S., Pellegrino, S., "Compliant Bistable Dielectric Elastomer Actuators for Binary Mechatronic Systems," Accepted for IDECT/CIE 2005 ASME Mechanism and Robotics Conference, 24-28 September 2005, Long Beach, California, USA.

50 Podder, T.K., J. Sherman, D.P. Clark, E.M. Messing, D.J. Rubens, J.G. Strang, L. Liao, R.A. Brasacchio, Y. Zhang, W.S. Ng, and Y. Yu, "Evaluation of Robotic Needle Insertion in Conjunction with in Vivo Manual Insertion in the Operating Room," IEEE International Workshop on Robots and Human Interactive Communication, pp. 66-72, 2005.

51 Roebuck, J., Ph.D., M.D., Brigham and Women's Hospital, Private Communications, 2005-2007.

52 Roth, B., Rastegar, J., Scheinman, V., "On the Design of Computer Controlled Manipulators," in First CISM-IFToMM Symposium on Theory and Practice of Robots and Manipulators, pp. 93-113, 1973.

53 Slocum, A., Precision Machine Design, Society of Manufacturing Engineers, 1992.

54 Song, S.K., Qu, Z., Garabedian, E.M., Gordon, J.I., Milbrant, J., Ackerman, J.J.H., "Improved Magnetic Resonance Imaging Detection of Prostate Cancer in a Transgenic Mouse Model," Cancer Research, Vol. 62, pp. 1555-1558, 2002.

55 Stoianovici, D., "Multi-imager compatible actuation principles in surgical robotics," Int J Medical Robotics and Computer Assisted Surgery, Vol 1(2), pp. 86-100, 2005.

56 Stoianovici, D., "Robotic Surgery," World Journal of Urology, Vol. 18, pp. 289-295, 2000.

57 Stoianovici, D., Patriciu, A., Petrisor, D., Mazilu, D., Kavoussi, L., "A New Type of Motor: Pneumatic Step Motor," IEEE/ASME Transactions on Mechatronics, Vol. 12, pp. 98-106, 2007.

58 Stoumbakis, N., Cookson, M.S., Reuter, V.E., Fair, W.R., "Clinical significance of repeat sextant biopsies in prostate cancer patients," Urology, Vol 49 (3A Suppl), pp. 113-118, 1997.

59 Strang, G., Introduction to Applied Mathematics, Wellesley-Cambridge Press, 1986.

60 Sujan, V., Lichter, M., Dubowsky, S., "Lightweight Hyper-redundant Binary Elements for Planetary Exploration Robots," Proc. 2001 IEEE/ASME International Conference on Advanced Intelligent Mechatronics (AIM '01) 811, Como, Italy, July 2001.

61 Taillant, E., Avila-Vilchis, J.C., Allegrini, C., Bricault, I., Cinquin, P., "CT and MR Compatible Light Puncture Robot: Architectural Design and First Experiment," Medical Image Computing and Computer-Assisted Intervention, pp. 145-152, 2004.

62 Tempany, C., M.D., Brigham and Women's Hospital, Private Communications, 2007.

63 Tsekos, N.V., Özcan, A., Christoforou, E., "A Prototype Manipulator for Magnetic Resonance-Guided Interventions Inside Standard Cylindrical Magnetic Resonance Imaging Scanners," Journal of Biomechanical Engineering, Vol 127, Issue 6, pp. 972-980, November 2005.

64 Vogan, J., Wingert, A.,. Hafez, M., Plante, J.S., Dubowsky, S., Kacher, D., Jolesz, F., "Manipulation in MRI Devices Using Electrostrictive Polymer Actuators: with an Application to Reconfigurable Imaging Coils," in 2004 IEEE International Conference on Robotics and Automation, vol. 2004, pp. 2498-2504.

65 Wan, G., Z. Wei, L. Gardi, D.B. Downey, and A. Fenster, "Brachytherapy needle deflection evaluation and correction," Medical Physics, Vol. 32, No. 4, pp. 902-909, 2005.

66 Warner, E., Plewes, D.B., Shumak, R.S., Catzavelos, G.C., Di Prospero, L.S., Yaffe, M.J., Goel, V., Ramsay, E., Chart, P.L., Cole, D.E.C., Taylor, G.A., Cutrara, M., Samuels, T.H., Murphy, J.P., Murphy, J.M., Narod, S.A., "Comparision of Breast Magnetic Resonance Imaging, Mammography, and Ultrasound for Surveillance of Women at High Risk for Hereditary Breast Cancer, *Journal of Clinical Oncology*, Vol. 19, pp. 3524-3531, 2001.

67 Wendt, O., Oellinger, J., Luth, TC., Felix, R., Boenick, U., "The effects of the use of piezoelectric motors in a 1.5-Tesla high-field magnetic resonance imaging system (MRI)," Biomed Tech, 2000.

68 Wingert A., "Development of a Polymer-Actuated Binary Manipulator", M.S. Thesis, Department of Mechanical Engineering, Massachusetts Institute of Technology, Cambridge, MA, 2002.

69 Wingert, A., Lichter, M., Dubowsky, S., "On the Design of Large Degree-of-Freedom Digital Mechatronic Devices Based on Bistable Dielectric Elastomer Actuators," in IEEE/ASME Transactions on Mechatronics, vol. 11, pp. 448 – 456,.August 2006.

70 Wingert, A., Lichter, M.D., Dubowsky, S. "On the Kinematics of Parallel Mechanisms with Bi-Stable Polymer Actuators." Proceedings of the 8th International Symposium on Advances in Robot Kinematics, Barcelona, Spain, June 2002.

71 Xiao, D., Phee, L., Yuenn, J., Chan, C.F., Liu, F., Ng, W.S., Ho, H., Thng, C.H., Tan, P.H., Cheng, C., "Software Design of Transperineal Prostate Needle Biopsy Robot," Proceedings of IEEE Conference on Control Applications, pp. 13-18, 2005.

72 Xuan, J., Wang, Y., Sesterhenn, I.A., Moul, J.W., Mun, S.K., "3-D Model Supported Prostate Biopsy Simulation and Evaluation," Medical Image Computing and Computer-Assisted Intervention, 1998.

73 Yuen, J.S.P., Thng, C.H., Tan, P.H., Khin, L.W., Phee, S.J.L., Xiao, D., Lau, W.K.O., Ng, W.S., Cheng, C.W.S., "Endorectal Magnetic Resonance Imaging and Spectroscopy for the Detection of Tumor Foci in Men with Prior Negative Transrectal Ultrasound Prostate Biopsy," *The Journal of Urology*, Vol. 171, pp. 1482-1468, 2004.

APPENDIX

A

DETAILS OF ACTUATOR AND MANIPULATOR DESIGN

A.1 Introduction

The details of the bistable actuators and the manipulator are discussed using dimensioned drawings.

A.2 Actuator Design Details

Figure 56 shows the bistable actuator module.

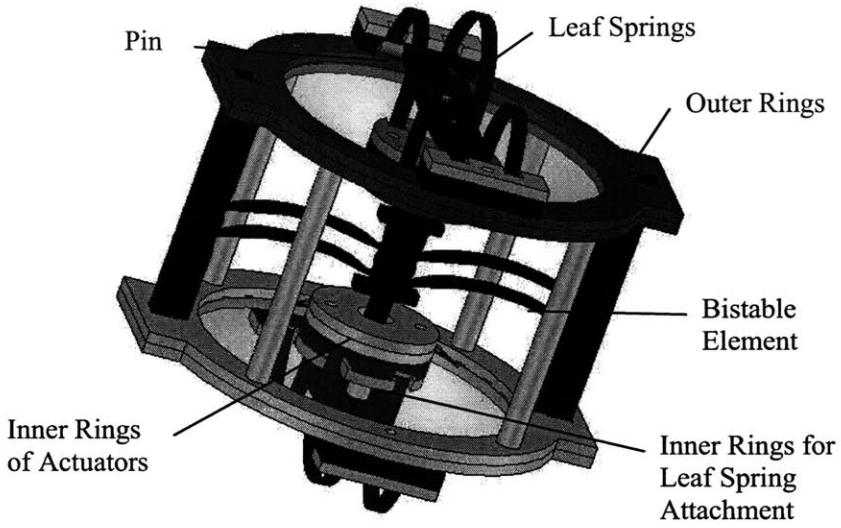

Figure 56: Bistable actuator

The outer ring of the actuators uses 3mm thick acrylic as shown in Figure 57. The slots for inserting the bistable element are larger than the edges of the bistable elements (5mm, see Figure 58) as discussed in Section 3.4. The inner diameter of the outer ring is 90mm and the outer diameter of the inner ring is 35mm [47].

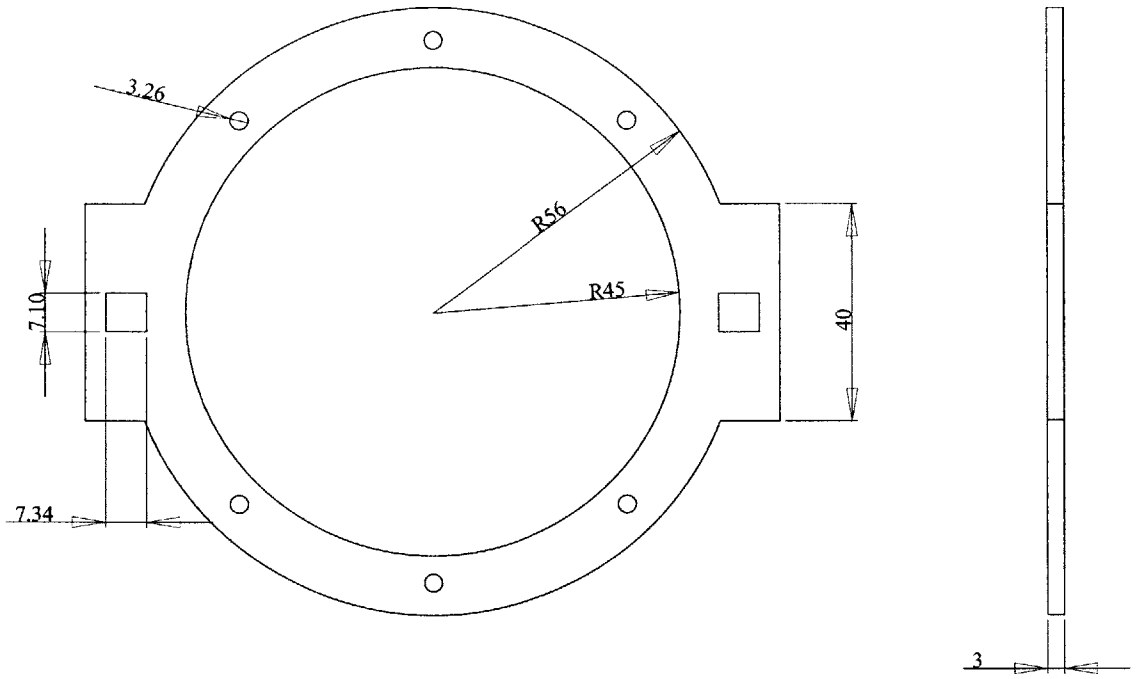

Figure 57: Outer ring of actuator

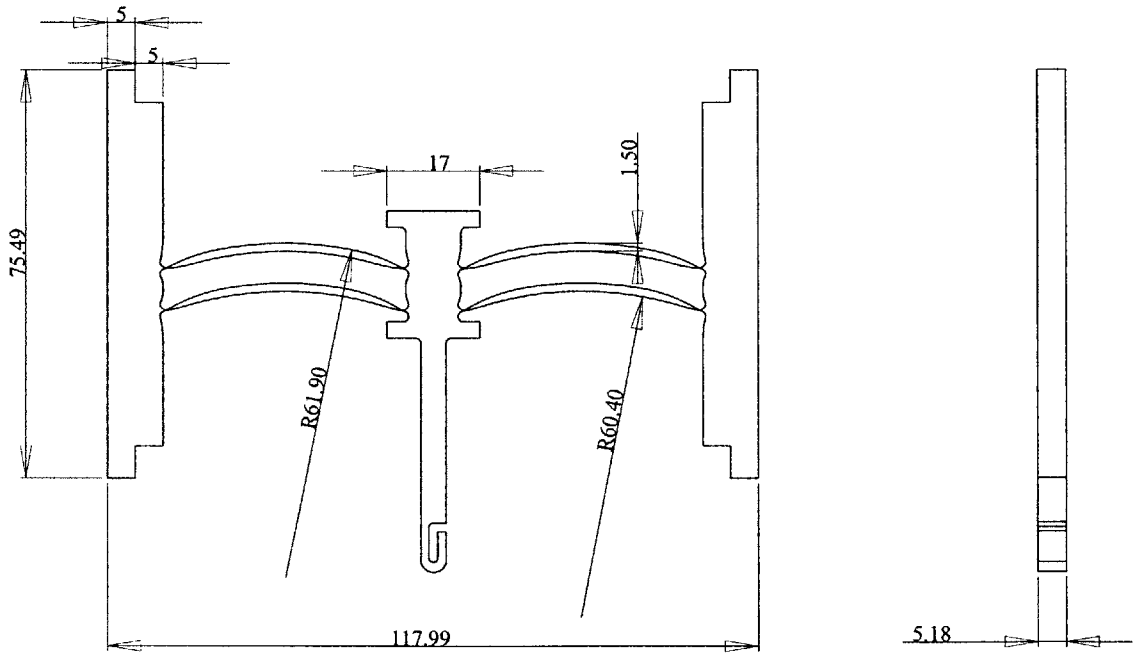

Figure 58: Bistable element

The inner rings of the inner circle of actuators have an axial hole to accommodate the bistable element (see Figure 59). The 10mm diameter ensures that the 5.2 x 5mm portion of the bistable element that runs through the hole does not rub against the actuator.

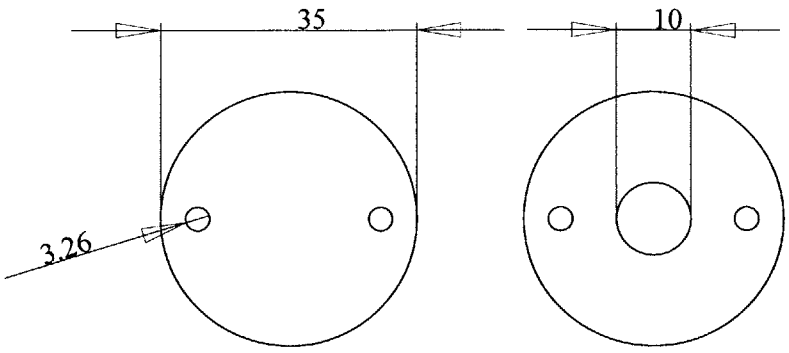

Figure 59: Inner rings of actuators far from center of planes (left) and close to center of planes (right)

The leaf springs are cut into of 3 x 76mm long strips of 0.41mm thick carbon fiber. They are then inserted into the slot in pin shown in Figure 60 and glued into place. The two rings are attached to the inner rings in Figure 59 making a slot for the pins to sit in that is too narrow for the leaf springs to come out of given the direction of their forces. The pins, attached to the leaf springs, are then inserted into the slots. The other ends of the leaf springs are inserted to identical slots on the outer rings.

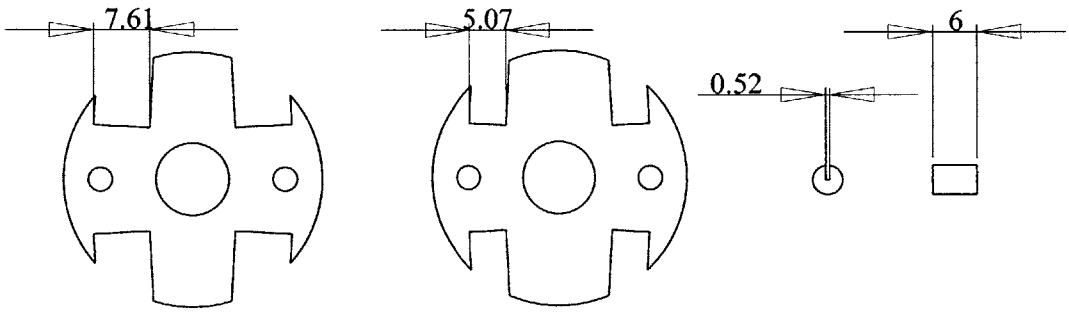

Figure 60: Inner rings and pin for leaf spring attachment

The leaf springs, after being inserted into their respective slots, are 42mm from end to end in the front plane and 14mm in the side plane. Figure 61 shows this initial required deformation of the inner versus outer rings of 14mm.

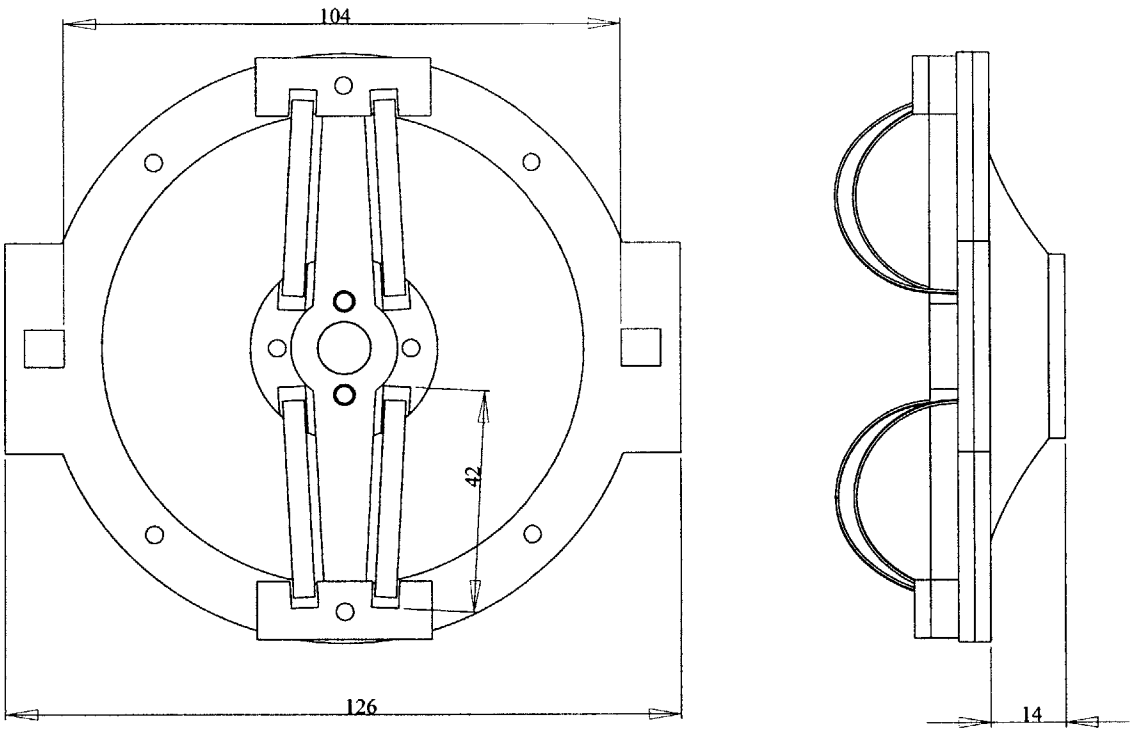

Figure 61: Actuator with hole for bistable element

A.3 Laboratory Manipulator Design

Each actuator is inserted into slots between two 6.35mm thick sheets of acrylic shown in Figure 62. The sheets are bolted together so that the distance between the planes can vary slightly. This is what holds the bistable elements at a certain force profile.

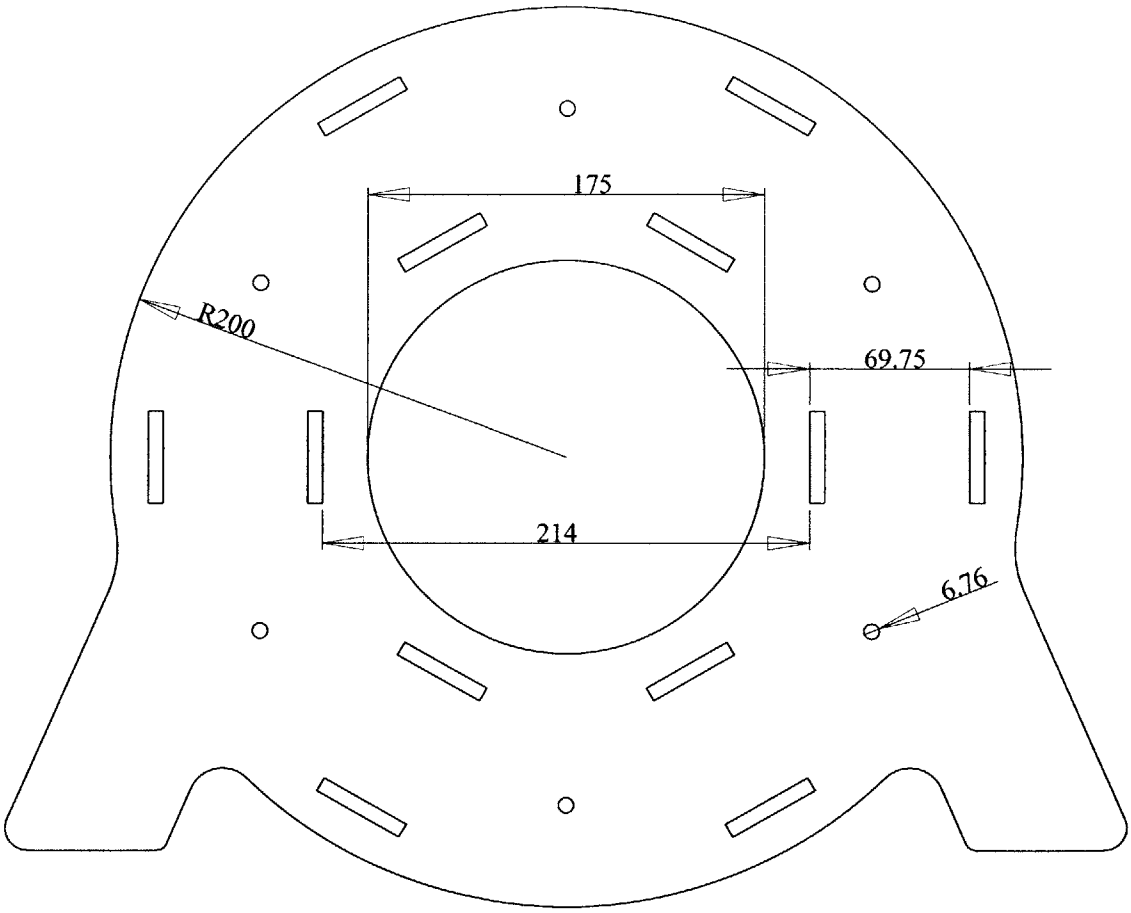

Figure 62: Plane to attach actuators

The springs are attached from the ends of the bistable elements to the center of the entire device shown in Figure 63. For the laboratory prototype, the original center piece was made out of carbon fiber with a large diameter to allow for easy rotation of a needle. Future designs will likely be modified to conform to the design of the insertion device.

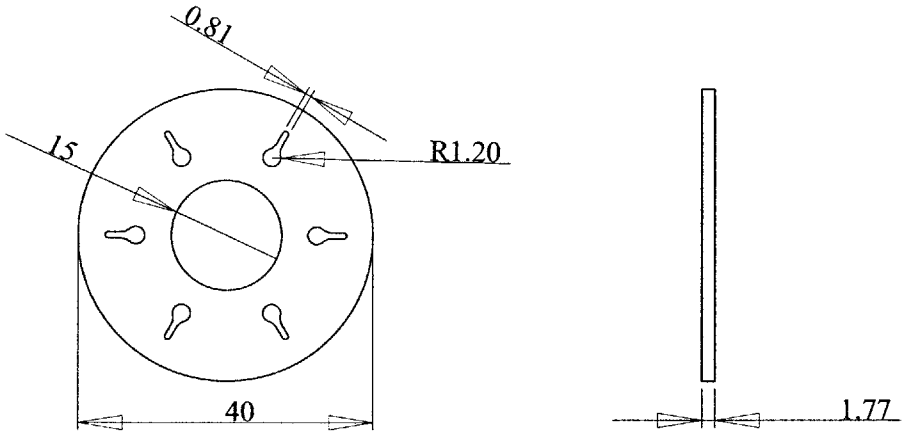

Figure 63: Center of plane

A.4 Fabrication

The actuators are designed for ease of manufacturing and safety during construction and testing. The bistable elements are cut on a numerically controlled mill. All other parts are laser cut.

Figure 64 shows the design for actuators. One of the actuators has a hole in the middle (a) to allow for connecting of the bistable elements to the rest of the system. These actuators are place closer to the center of the plane. The actuators in the outer circle of the device do not require this hole (b).

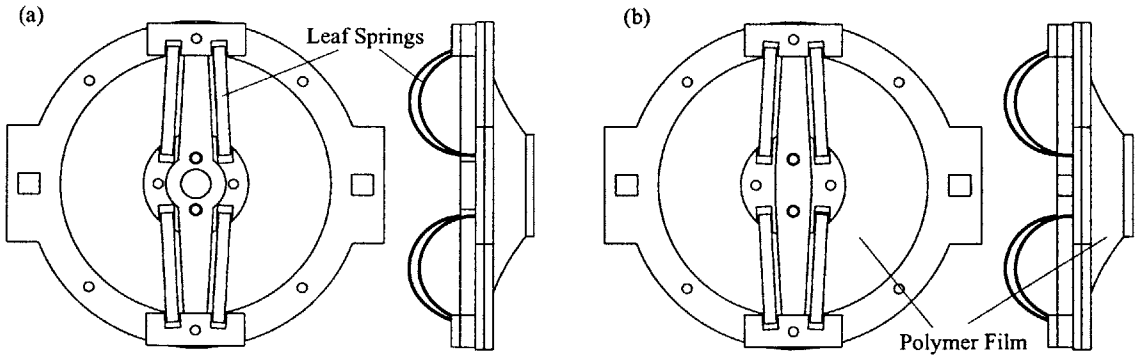

Figure 64: Actuators with (a) and without hole (b)

The actuators are attached to the bistable device using spacers as shown in Figure 65. Both actuators are used independently of each other for the forward and return strokes. Imperfections due to manufacturing by hand often result in early actuator failure. The ability to easily replace actuators in the laboratory prototype made for much quicker assembly and repair.

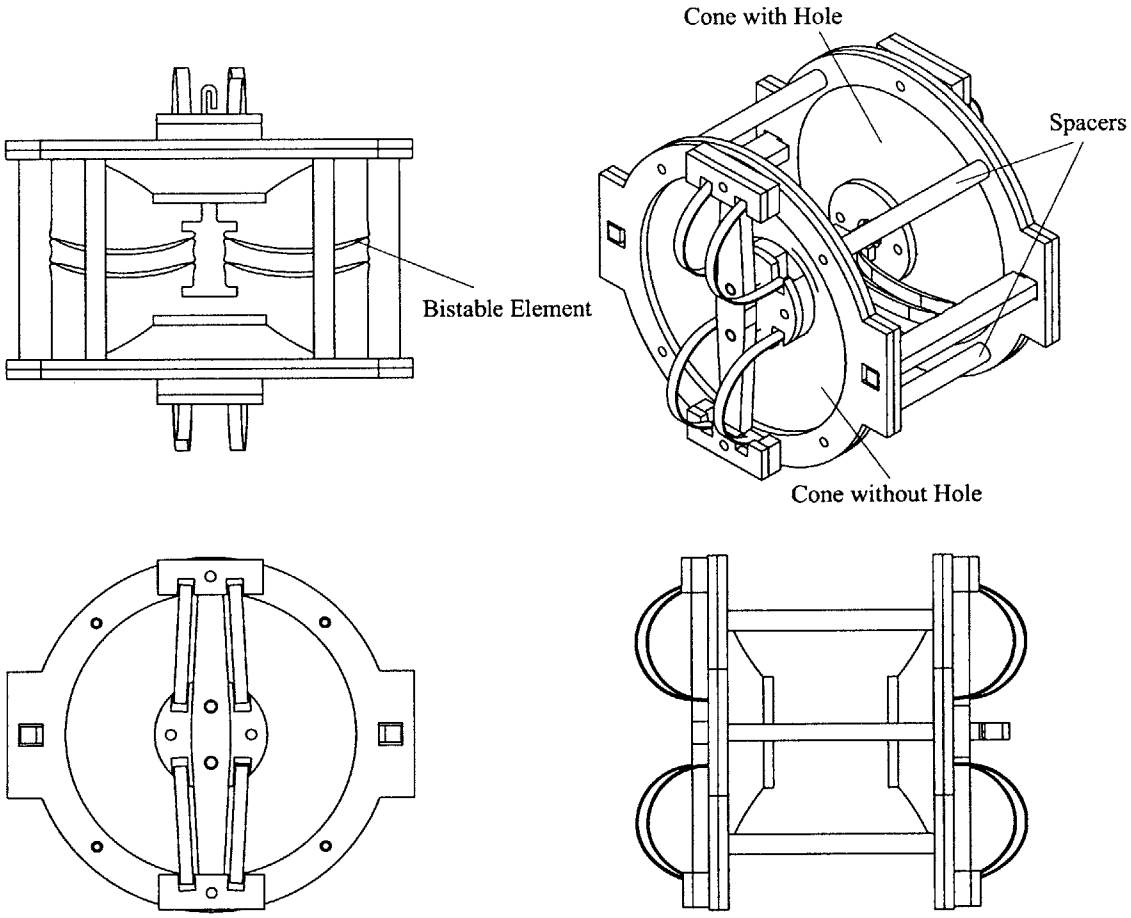

Figure 65: Bistable actuator

The actuators must be preloaded in order to obtain useful motion. Carbon fiber leaf springs are used because their force profile compliments that of the actuators [47]. Acrylic pins were cut with a slot to insert the end of the leaf springs. The leaf springs were glued to the pins using cyanoacrylate and set into slots on the actuator to allow for free, but safe, rotation of the

leaf springs as shown in Figure 66. This greatly reduced assembly time and ensured the leaf springs would not become detached from the assembly.

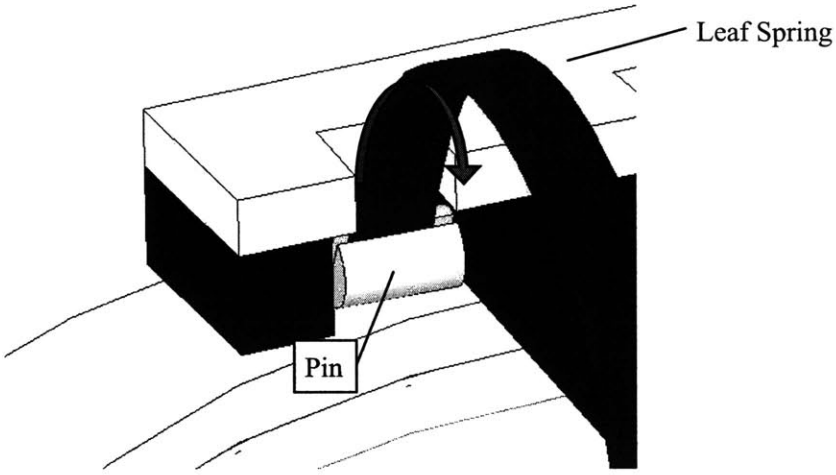

Figure 66: Leaf spring attachment using acrylic pin